High-resolution characterization of the aging brain using simultaneous quantitative susceptibility mapping (QSM) and R_2* measurements at 7 Tesla

Matthew J Betts[1*], Julio Acosta-Cabronero[1*], Arturo Cardenas-Blanco[1,2], Peter J Nestor[1], Emrah Düzel[1,2,3]

[1] German Center for Neurodegenerative Diseases (DZNE), Magdeburg, Germany
[2] Institute of Cognitive Neurology and Dementia Research, Otto-von-Guericke University Magdeburg, Leipziger Str. 44, 39120 Magdeburg, Germany
[3] Institute of Cognitive Neuroscience, University College London, 17 Queen Square, London, WC1N 3AR, UK

* Both authors contributed equally to this work.

Corresponding author: Dr Matthew J Betts
Corresponding author's address: Deutsches Zentrum für Neurodegenerative Erkrankungen e.V. (DZNE) c/o Universitätsklinikum Magdeburg, Leipziger Strasse 44, Haus 64, 39120 Magdeburg, Deutschland
Corresponding author's phone and fax: Tel. +49 391 67-25058; Fax +49 391 67-25060
Corresponding author's e-mail address: matthew.betts@dzne.de

Conflict of interest: The authors declare no competing financial interests

Keywords: brain iron; brain mineralization; aging; quantitative susceptibility mapping; R_2* mapping; cortex; subcortical grey matter; white matter

ABSTRACT

Quantitative susceptibility mapping (QSM) has recently emerged as a novel magnetic resonance imaging (MRI) method to detect non-haem iron deposition, calcifications, demyelination and vascular lesions in the brain. It has been suggested that QSM is more sensitive than the more conventional quantifiable MRI measure, namely the transverse relaxation rate, R_2*. Here, we conducted the first high-resolution, whole-brain, simultaneously acquired, comparative study of the two techniques using 7 Tesla MRI. We asked which of the two techniques would be more sensitive to explore global differences in tissue composition in elderly adults relative to young subjects. Both QSM and R_2* revealed strong age-related differences in subcortical regions, hippocampus and cortical grey matter, particularly in superior frontal regions, motor/premotor cortices, insula and cerebellar regions. Within the basal ganglia system—but also hippocampus and cerebellar dentate nucleus—, QSM was largely in agreement with R_2* with the exception of the globus pallidus. QSM, however, provided superior anatomical contrast and revealed age-related differences in the thalamus and in white matter, which were otherwise largely undetected by R_2* measurements. In contrast, in occipital cortex, age-related differences were much greater with R_2* compared to QSM. The present study, therefore, demonstrated that *in vivo* QSM using ultra-high field MRI provides a novel means to characterize age-related differences in the human brain, but also combining QSM and R_2* using multi-gradient recalled echo imaging can potentially provide a more complete picture of mineralization, demyelination and/or vascular alterations in aging and disease.

1. INTRODUCTION

Iron is involved in numerous fundamental neural processes such as oxygen transportation, DNA synthesis, mitochondrial respiration, myelin production as well as synthesis and metabolism of neurotransmitters (Ward et al., 2014). In aging, selective accumulation of iron—largely bound to ferritin and neuromelanin—occurs in numerous brain regions with possible neurotoxic consequences such as oxidative damage and cell death (Ward et al., 2014). Whilst the mechanisms underlying this accumulation are not yet fully understood, measuring brain iron may provide an important insight into understanding the neurodegenerative processes occurring in aging and neurological disease.

Previous studies using either *post mortem* (Hallgren and Sourander, 1958) or *in vivo* iron-sensitive MRI techniques (Acosta-Cabronero et al., 2016; Bartzokis et al., 2007; Haacke et al., 2007; Hasan et al., 2012; Pfefferbaum et al., 2009; Raz et al., 2007) have revealed that iron levels and its rate of accumulation are heterogeneous in the human brain. Furthermore, iron deposition may correlate with cognitive impairment (Daugherty et al., 2015; Ghadery et al., 2015; Penke et al., 2012) and slowing of motor performance (Cass et al., 2007; Li et al., 2015; Sullivan et al., 2009), though it is unclear whether this is cause or consequence. Since aging is the major risk factor for many neurodegenerative diseases, age-related accumulation of iron may be an important factor that contributes to

neurodegenerative pathology (Ward et al., 2014). This notion has been supported by *post mortem* and *in vivo* human studies identifying abnormal iron deposition in neurodegenerative diseases such as Alzheimer's disease (AD) (Cornett et al., 1998; Bartzokis et al., 2000) and Parkinson's disease (PD) (Bartzokis et al., 1999; Bunzeck et al., 2013; Sofic et al., 1991).

To date, the T_2* transverse relaxation time, or its inverse rate, R_2* (=1/T_2*), has been routinely utilised as a surrogate marker to assess brain iron deposition with both *in vivo* (Gelman et al., 1999; Péran et al., 2009; Yao et al., 2009) and *post mortem* data (Langkammer et al., 2010), demonstrating a linear relationship between R_2* and iron concentration in deep grey matter (GM). R_2*, however, is known to be a composite measure sensitive to T_2/diffusion effects and magnetic field inhomogeneities. R_2* can be driven by intravoxel spin dephasing in the vicinity of steep field gradients (Fernández-Seara and Wehrli, 2000) stemming from the focal mineralization of deep GM nuclei; it is also vulnerable to spurious observations from external sources such as air in cranial cavities and other non-local field disturbances (Deistung et al., 2013). Recently, a novel technique termed quantitative susceptibility mapping (QSM) has been proposed to try to overcome the non-locality of magnetic field fluctuations. QSM provides a quantitative and local anatomical contrast by estimating magnetic susceptibility sources from their signature on the MRI signal phase (de Rochefort et al., 2008). QSM results have shown agreement with both *post-mortem* iron measurements (Langkammer et al., 2012; Sun et al., 2015; Zheng et al., 2013) and additional iron-sensitive MRI techniques (Bilgic et al., 2012; Poynton et al., 2015). Furthermore, at ultra high-field strength (B_0≥7 Tesla), QSM has demonstrated superb anatomical contrast and superior delineation of GM substructures compared to R_2* and conventional iron-sensitive measures (Deistung et al., 2013; Lotfipour et al., 2012).

Studies comparing QSM and R_2* as surrogate markers of brain iron deposition within cortical regions of healthy young individuals (Deistung et al., 2013) and in subcortical regions in PD (Barbosa et al., 2015), have shown QSM may provide superior sensitivity to detect differences in local GM. No study to date, however, has directly compared QSM and R_2* differences as a result of normal aging. Furthermore both aforementioned studies were limited to regions-of-interest (ROI) analyses. Yet, recent aging lifespan studies using quantitative multimodal MRI (Callaghan et al., 2014) and QSM (Acosta-Cabronero et al., 2016) have shown whole-brain analyses may be used to reveal global patterns of iron distribution that may otherwise be missed in pre-defined ROI analyses.

A direct whole-brain comparison of QSM and R_2* is important not only because they may show differential sensitivity to age-related differences in iron-rich brain regions, but also because they may be differentially affected by additional pathological processes. Both are also substantially affected by variations in myelin density, however in contrasting ways. R_2* increases proportionally to the concentration of both iron (Langkammer et al., 2010) and myelin (Lee et al., 2012), whilst the two substances exert opposing effects on magnetic susceptibility (Liu et al., 2011; Schweser et al., 2011) due to the strong diamagnetic component driven by phospholipids in myelin membranes

(Langkammer et al., 2012; Li et al., 2012). QSM and R_2* are, therefore, unique and potentially complimentary contrasts to explore whole brain age-related differences, chiefly owing to their differential sensitivities to iron and myelin content (Fukunaga et al., 2010); they may also be differentially modulated by other forms of mineralization such as calcifications (Chen et al., 2014), by brain oxygen-saturation levels (Rodrigue et al., 2011) and/or vascular pathology (Reichenbach et al., 2015).

Here, we conducted the first high-resolution, whole-brain, simultaneously acquired, comparative QSM versus R_2* imaging study using 7 Tesla (7T) MRI. QSM and R_2* measurements—inferred from the same multi-gradient recalled echo (GRE) acquisition—were first qualitatively compared using a whole-brain cluster-wise approach, and were then more directly contrasted with data extracted from a whole-brain ROI parcellation.

2. METHODS

2.1 Study subjects

A total of 20 healthy older adults aged 64 to 75 years of age (mean: 70 ± 1; 11 females and 9 males, years of education: 16 ± 3) and 20 younger adults aged 22 – 28 years of age (mean: 24 ± 2; 11 females and 9 males) were recruited, and written informed consent was obtained from all participants in accordance with the Declaration of Helsinki. The study received ethical approval from the Faculty of Medicine at the University of Magdeburg. All older adults were a subset of a larger cohort previously screened to ensure intact global cognitive performance using a brief neuropsychological battery, exclude neurological or major psychiatric illness and cases of white matter (WM) ischaemia (Acosta-Cabronero et al., 2016). Prior to recruitment into this study, T_2-weighted images acquired with 3T MRI were visually inspected to exclude severe brain abnormalities. Vascular pathology was assessed on T_2-weighted MRI by applying the Fazekas scale (Fazekas et al., 1987) whereby deep or periventricular scores of ≥2 were excluded. Mild lesions (i.e. small, probable calcium deposits), however, were not excluded and deemed a feature of normal aging. No subjects demonstrated evidence of micro-haemorrhages. Data on vascular risk factors was collected from all subjects, namely history of hypertension, heart attack and diabetes in addition to height and weight. Two older participants had been diagnosed with hypertension and one subject was obese (body-mass index >30). No subjects had history of diabetes or heart attack.

2.2 Imaging protocol

All subjects were scanned on a Siemens MAGNETOM 7T system using a Nova Medical (Willmington, MA) 32-channel reception head-coil. Whole-brain susceptibility weighted imaging (SWI) consisted of a 3D GRE sequence with four monopolar readouts centred at 8, 13, 18 and 23 ms after (3D slab-selective) excitation; receiver bandwidth was 300 Hz/pixel for each acquired echo. Note that only the first echo was fully flow compensated. Additional imaging parameters were: repetition time (TR)=28 ms; flip angle=12°; 3D matrix

dimensions, 320×320×88 (straight-axial slices) and voxel size, 0.8×0.8×1.6 mm^3, with 7/8 phase and slice k-space undersampling giving a scan time of 10:05 minutes. The prescribed matrix size ensured whole-brain coverage, while large voxels prioritised contributions from non-venous structures with high signal-to-noise ratio. The distinct advantage of this multi-echo approach is that quantitative R_2* maps and QSM can be reconstructed from the same dataset, readily enabling direct comparison between both measurements. The disadvantages, however, are that flow effects are more apparent than in single-echo fully flow compensated acquisitions, and that blurring due to subject motion or phase errors are more prevalent due to longer readout and total scan times.

A T_1-weighted 3D-MPRAGE was also acquired in the same scanning session to independently resolve the underlying brain anatomy. The following acquisition parameters were used: inversion time of 1050 ms; flip angle was 5°; echo time (TE) of 2.09 ms; receiver bandwidth was 230 Hz/pixel; echo spacing was 6.1 ms; and TR=2000 ms. 3D matrix dimensions were 320×320×224 (straight-sagittal slice orientation with 0.5-mm inter-slice gap), 7/8 partial Fourier, and 0.8×0.8×0.8 mm^3 voxel size. GRAPPA was also enabled with acceleration factor of 2 and 32 reference lines.

To minimise motion and increase inter-subject reproducibility in positioning, a thin pillow was placed on the base of the coil surrounding the sides and the back of the head.

2.3 QSM reconstruction

In order to reduce phase errors in the combination of multi-echo data, we estimated the off-resonance frequency from the complex GRE signal evolution by solving a nonlinear least-squares fitting problem (Liu et al., 2013). Phases were subsequently unwrapped with a direct continuous Laplacian method (Schofield & Zhu, 2003), although one must note this method may introduce some errors in the vicinity of vasculature (Haacke et al., 2015). Then, locally sourced inductions (i.e. foreground field shifts) were revealed through background field extraction with the SHARP algorithm (sphere radius of 5 mm; Schweser et al., 2011). Prior to applying SHARP, BET2 (Smith, 2002) with fractional threshold set to 0.2 was used to estimate the brain boundary from the radio-frequency (RF) bias-corrected (Tustison et al., 2010) T_2*-weighted, combined magnitude image. Finally, for conditioning the susceptibility restoration problem from the background-field corrected phase images, the iterative, morphology-enabled, non-linear dipole inversion (MEDIN) solver with dynamic model error reduction (MERIT) was applied (Liu et al., 2013) – source code available from: http://weill.cornell.edu/mri/pages/qsm.html. MEDIN incorporates the ℓ_1-norm of a total-variation operation to the susceptibility distribution as a penalty to "compartmentalize" (by encouraging sparsity) an otherwise data-consistent solution. The regularising term was also aided by morphological information, i.e. element-wise multiplication with a gradient mask conforming to the 30% greatest GRE magnitude gradients. The regularisation parameter (λ=1,000) was the median resulting from five randomly selected datasets, where—using λ=500

steps—the consistency-term residual was matched to an estimate of the foreground field noise level (Morozov, 1966). Note that with the exception of the initial multi-echo combination step, the reconstruction pipeline is essentially the same as that described in a recent 3T study (Acosta-Cabronero et al., 2016).

2.4 QSM reference normalization

The magnetic dipole kernel operation used for inversion eliminates direct current (or DC) offsets; thus, QSM values are typically normalized to a reference region in an attempt to re-adjust such an offset. Note, however, that there is no consensus at present on reference-region selection. Whilst manual selection may introduce inconsistency, automated methods are yet to be proposed. In a previous study, we demonstrated that aging effects on QSM far outweigh the impact of such a reference adjustment (Acosta-Cabronero et al., 2016), indicating it is appropriate from a reproducibility standpoint, to report non-normalized values; nevertheless, we additionally performed the subsequent analyses with reference-normalized QSM values to independently confirm this observation. Normalization consisted of a direct subtraction by the median QSM value of a confluent region with low non-normalised variance. The reference region—located in parietal WM far from a GM/WM boundary—was traced with the aid of a study-wise map of QSM variance (relative to the population mean) saturated at an upper threshold of 0.005. Notably, in agreement with our previous 3T study, non-normalised signed QSM values revealed statistically comparable aging effect sizes to reference-normalised QSM data (Friedman's test; not significant; (χ^2 = 0.60; p = 0.439).

2.5 Absolute QSM

In the present study, we also propose taking the absolute value of signed QSM data as an alternative magnetic susceptibility related metric. The impact of this new approach is two-fold: (i) it renders QSM data more comparable to the positive-real nature of R_2* by additively collapsing effects from paramagnetic and diamagnetic substances into an unsigned measure of "mineralization"; but it also, (ii) reduces the spatial gradient of blooming effects often observed in susceptibility maps (i.e. residuals of the QSM inversion that originate from strongly reactive magnetic species such as iron). Taking the absolute to QSM values, thus, aimed at minimising the spurious impact that such boundary effects have both on regional extractions and on the application of a smoothing kernel (required to correct for co-registration errors and other imperfections prior to whole-brain analysis). It must be highlighted, however, that the disadvantage of absolute QSM is that it cannot distinguish greater diamagnetism (e.g. calcifications) from greater paramagnetism (e.g. iron deposition); it cannot tell, thus, the type of mineralisation. Notably, we found subcortical effect size differences between signed QSM and absolute QSM data in the present aging cohort (χ^2 = 52.27; p<0.001), which suggest they might be capturing differential magnetostatic interactions of counteracting species such as iron and calcium or myelin. Both metrics were thus studied and interpreted in combination. In addition, in order to provide further insights into the exact

(diamagnetic/paramagnetic) origins of age-related effects, positive-only and negative-only QSM maps were also analysed.

2.6 R_2 mapping*

MR signal decays across four T_2* weighted images were (voxel-by-voxel) fitted to a mono-exponential model ($S=S_0\, e^{-TE/T_2^*}$) using a previously validated, non-linear least-squares fitting routine (Acosta-Cabronero and Hall, 2009). For robustness, starting values were approximated with a linear fit on the logarithm of the signal magnitude of the first two echoes. One should note, however, that numerous studies have described the deleterious impact of noise in scenarios of low signal where the Rician nature of the signal magnitude may artificially elevate true values (Gudbjartsson and Patz, 1995; Cardenas-Blanco et al., 2008). In particular at ultra-high field, such scenarios may unfold for late echoes, potentially resulting in the underestimation of R_2* values. In order to assess whether such bias affected our measurements, a large rectangular noise region (280×20) outside the brain posteriorly—avoiding contamination along the phase-encoding direction—was selected (see Inline Supplementary Fig. 1A), and the noise floor was set to 7 times the standard deviation of the real signal in this region ($7\sigma_G$). The same noise region was used for all subjects, ensuring through visual inspection its correct placement. For all iron-rich nuclei studied here, signal magnitude at the last echo, i.e. TE=23 ms, was greater than the noise floor suggesting estimated R_2* values were unbiased by the effect of noisy signals (see Inline Supplementary Fig. 1B). Nevertheless, individual data points below the noise floor were excluded from the relaxometry calculation.

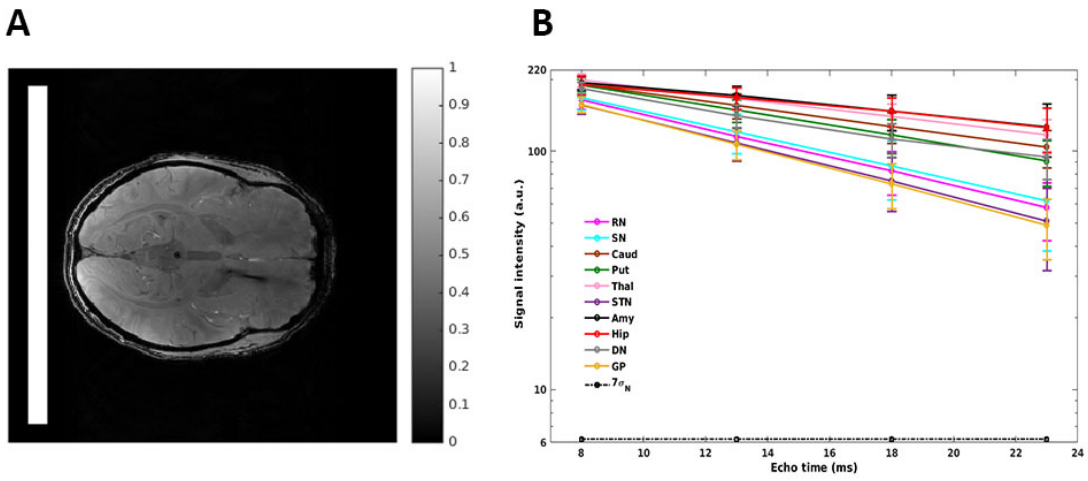

Inline Supplementary Figure 1. Data-quality assurance. (A) A large rectangular ROI in a posterior region outside the brain was selected to estimate the noise level. (B) Example signal decay quantified from four back-to-back gradient echoes (equally spaced every 5 ms from 8 to 23 ms) and plotted on a semi-logarithmic scale. Notably, the average T_2*-weighted signal for the globus pallidus (GP)—i.e. the brain structure with the shortest average T_2* value—remained well above the noise floor.

2.7 QSM and R_2 spatial standardisation*

RF-bias corrected with N4-ITK (Tustison et al., 2010) MPRAGE images were standardised (to a study-wise space) by way of a parallel routine for template calculation provided in ANTs v2.1 (Avants et al., 2008). Simultaneous co-registrations were driven by a cross-correlation minimization performed over three resolutions with a maximum of 90 iterations at the coarsest level, 30 at the next coarsest and 90 at full resolution; template update step size was set to 0.1 mm. Four rigid-then-affine iterations were followed by six full runs of the above non-linear multi-resolution routine to ensure stable convergence. Subsequently, bias-corrected T2*-weighted magnitude images for each SWI dataset were affine co-registered using ANTs to their corresponding MPRAGE volume. T_2*-weighted, R_2* and QSM spatial standardisation was achieved through the warp composition of the above transformations and third-order b-spline interpolation (average-population templates are shown in Inline Supplementary Fig. 2).

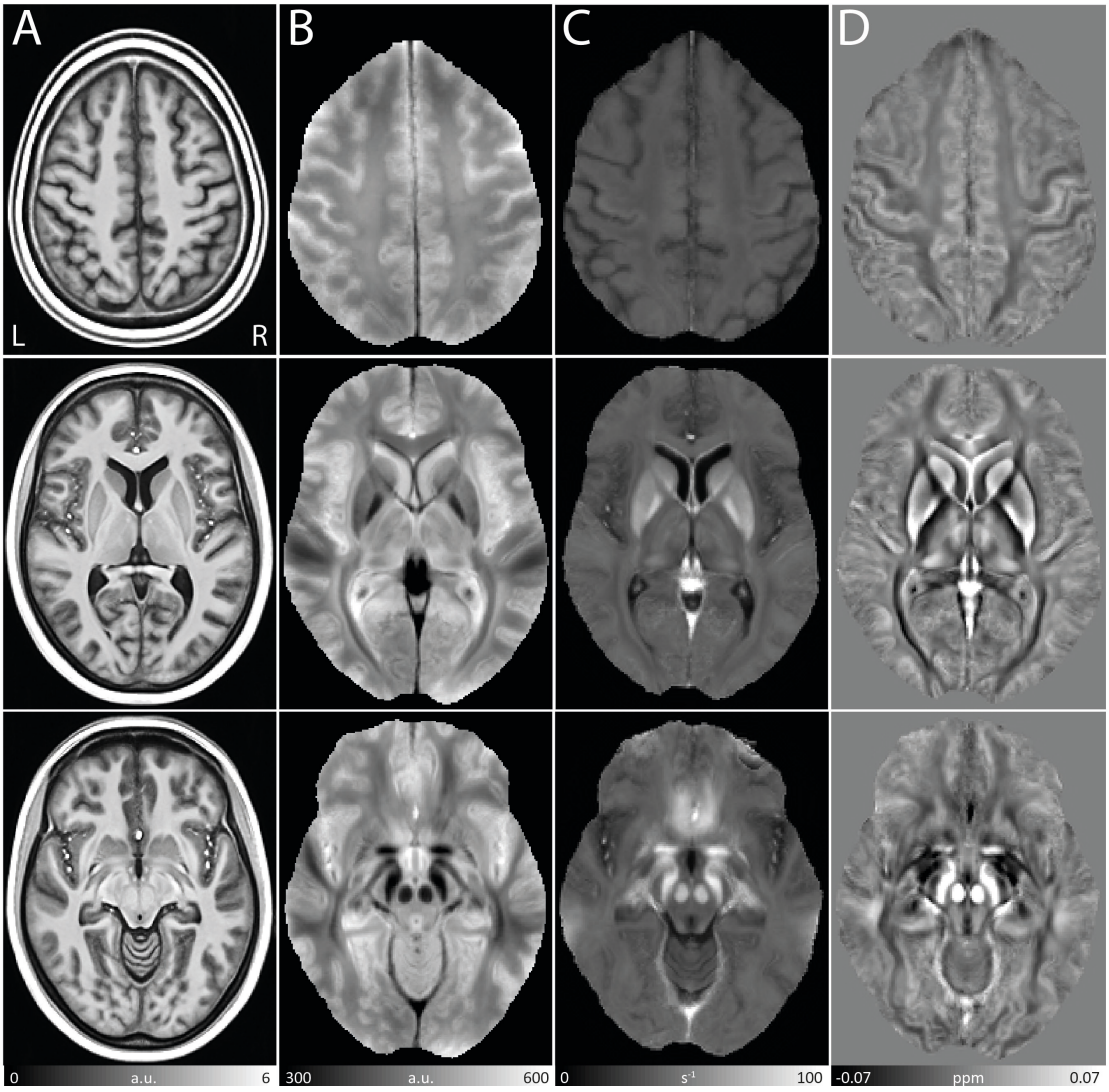

Inline Supplementary Figure 2. Study-wise templates for anatomical T_1-weighted MRI, T_2*-weighted MRI, transverse relaxation rate (R_2*) mapping and quantitative susceptibility mapping (QSM).

2.8 Co-registration performance and data dispersion

The analyses reported below strongly rely on the performance of the co-registration routine since warping inaccuracies arising from heterogeneous behaviors induced by atrophy, venous idiosyncrasies or imaging artifacts, may lead to abnormally high QSM variance. These errors, however, are characterised by the spatial distribution of unphysical high relative variances.
In this study, QSM variances were saturated at 5% (relative to the absolute mean across subjects), i.e. five times greater than that measured in the dentate nucleus – the subcortical structure with the greatest implicit variance (see Table 2 in the results section). As can be seen from mean and relative variance maps across N=40 subjects (plotted in Fig. 1), signed QSM returned the greatest variances chiefly near vasculature, and within or in the vicinity of several cortical areas (Fig. 1B). Except for the thalamus—composed of heterogeneous sub-nuclei—and hippocampus, all ROIs were devoid of large signed QSM deviations. Taking the absolute to QSM, as expected, resulted in reduced inter-subject variance across the cortex, though spurious dispersion could still be observed in the vicinity of the vasculature (Fig. 1D). R_2* yielded overall the slightest relative variances (Fig. 1F). Nevertheless, for all types of measurement, almost all subcortical ROIs including small structures such as the RN, SN and STN avoided overlapping structural boundaries and regions of high variance. The cortex was expected to be more problematic with signed QSM due to strong GM/WM susceptibility gradients. For absolute QSM and R_2*, however, the majority of the cortical ribbon was shown to be devoid of spurious variability due to less abrupt spatial variations – qualitatively illustrating their value to study the cortex with whole-brain analysis methods.

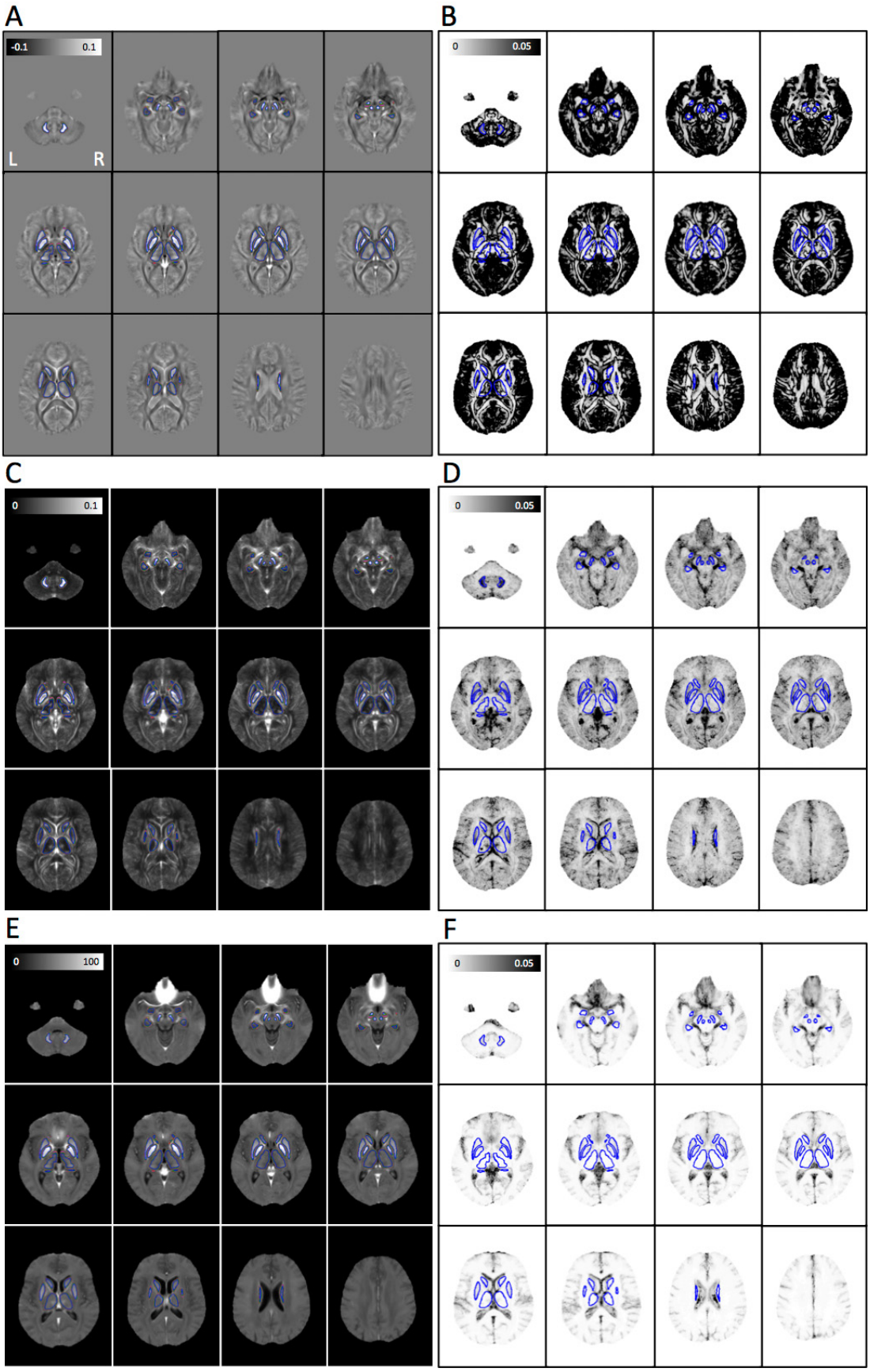

Figure 1. Mean and relative variance maps across N=40 subjects in study-wise space for (A, B) signed QSM, (C, D) absolute QSM and (E, F) R_2*, respectively. Blue

contours represent the subcortical regions of interest from which quantitative data was extracted in this study.

2.9 Whole-brain QSM and R_2 analyses*

Age differences were estimated for the whole brain by computing two-sample permutation statistics using Randomise v2.9 (Winkler et al., 2014) with threshold-free cluster enhancement (TFCE) (Smith and Nichols, 2009) and on the null hypothesis for each permutation that QSM/R_2* means are equal on both young and elderly groups. Cluster-based inferences were made through 5,000 permutations of the data at a family-wise error (FWE) corrected threshold level of 0.05 with default TFCE settings. Subsequently after analysis, the QSM template and study results were warped to MNI152 space (Montreal Neurological Institute, McGill University, Canada). The study-wise template to MNI152 transformation was estimated with a rigid, affine plus deformable b-spline co-registration routine in ANTs ('antsRegistrationSyN').

2.10 Impact of spatial smoothing on whole-brain analyses

It must be noted that spatial smoothing is common practice prior to whole-brain analyses to reduce both the deleterious effects of data dispersion due to misregistration and the overall number of independent statistical tests. QSM and R_2* data were, thus, smoothed by convolution with a 3D-Gaussian kernel prior to performing statistics. However, since this type of analysis is novel using QSM data, we also assessed the performance of a previously proposed smoothing-compensation strategy (Lee et al., 2009). The procedural steps were the following: (i) GM and WM tissue segments were inferred from native T_1-weighted images using the "unified segmentation" model built into SPM12 (http://www.fil.ion.ucl.ac.uk/spm/software/spm12) with default settings; (ii) both segments were added together resulting in a brain parenchymal probability segment, which was warped to the study-wise space, thresholded at Prob>0.5 and binarised; (iii) warped QSM and R_2* maps were subsequently brain-masked; and (iv) both brain masks and quantitative maps were smoothed with a 3D-Gaussian kernel; finally, (v) smoothed QSM/R_2* volumes were (element-wise) divided by their corresponding smoothed brain mask resulting in parenchyma-specific, smoothing-compensated maps. Four examples (data for two young and two elderly subjects) of unsmoothed and smoothed, warped QSM and R_2* maps are shown in Inline Supplementary Fig. 3. Fig. 2 illustrates the impact of such procedure in comparison with direct Gaussian blurring. Thus in this regard B, D and F correspond to the analyses presented in fig 5, 8 and 9 respectively. Qualitatively, the former appears to be desirable in that significant clusters were overall brain-specific, yet more widespread. This is most noticeable in signed QSM and R_2* analyses, whereas the same strategy on absolute QSM—partly devised to minimise the undesirable effects of CSF contamination—as expected, had a weaker impact. During this step, the newly implemented smoothing-compensation strategy was deemed superior and used in all subsequent analyses presented.

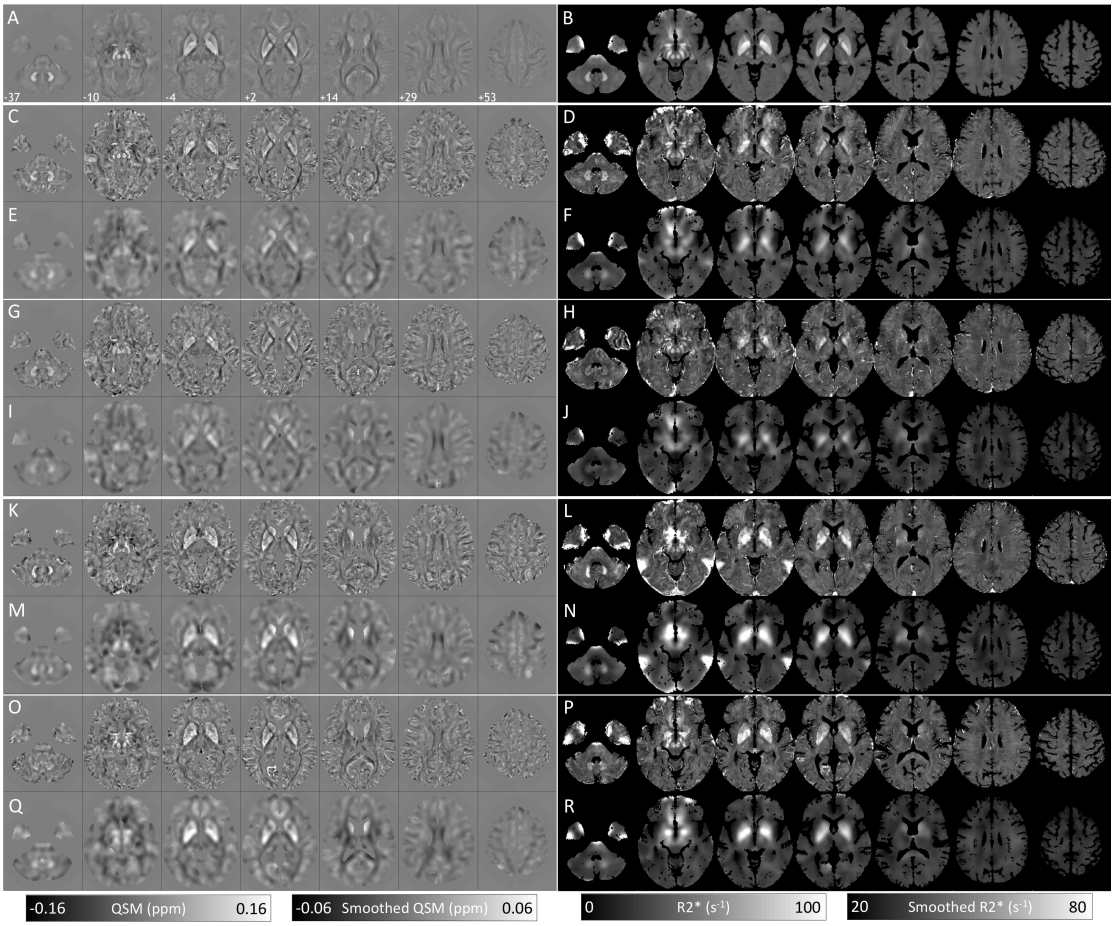

Inline Supplementary Figure 3. Axial cuts of spatially normalized QSM (left) and R_2* data (right). (A-B) Global mean maps. (C-D/G-H and K-L/O-P) Unsmoothed maps for two young and two elderly subjects, respectively. (E-F/I-J and M-N/Q-R) Smoothing-compensated data for the same subjects.

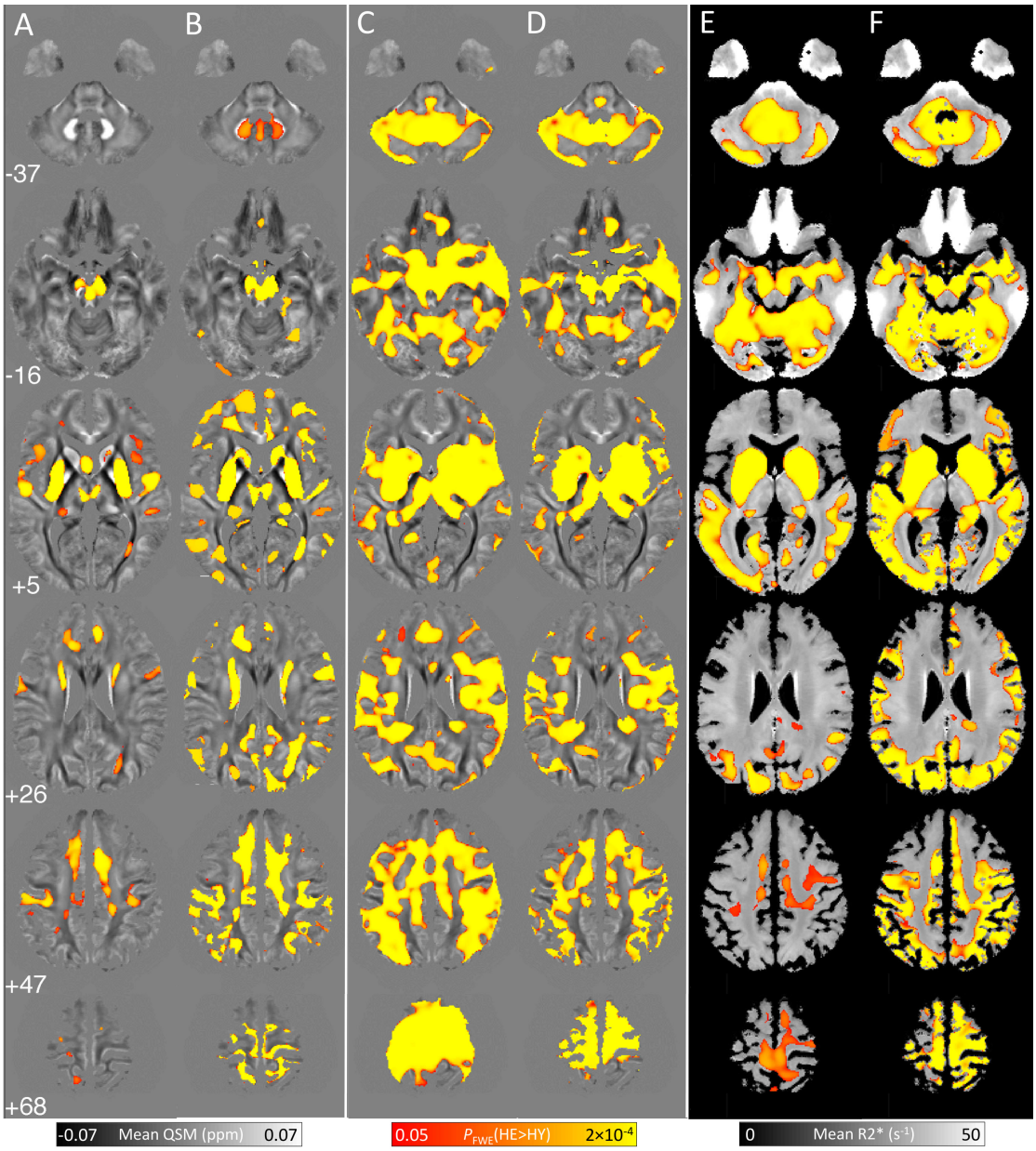

Figure 2. Qualitative comparison between smoothing methods. (A-B) Signed QSM, (C-D) absolute QSM and (E-F) R_2*. The left column of each pair represents results for elderly versus young comparisons with direct Gaussian smoothing (A, C and E); brain-specific, smoothing-compensated results are on the right side (B, D and F). Abbreviations: healthy elderly (HE), healthy young (HY).

The relationship between smoothing kernel width and cluster extent is also yet unknown for QSM data; thus, to provide some insight, we qualitatively compared results using three Gaussian kernels with standard deviation (sigma): 1.5, 3 and 5 mm (Fig. 3). As expected, blurring QSM/R_2* data improved both cluster sensitivity and spatial confluence, though the effect of kernel size was different across data type. For signed QSM, improvements were observed when increasing kernel width from 1.5- to 3-mm sigma, but a wider kernel appeared to

excessively blur away statistical effects. For absolute QSM data, we observed a monotonic increase in cluster extent as a function of kernel width; whereas for R_2* data, a plateau effect was observed for kernel widths of 3 mm and greater. We concluded that a Gaussian kernel width with standard deviation of 3 mm was appropriate in the context of this study.

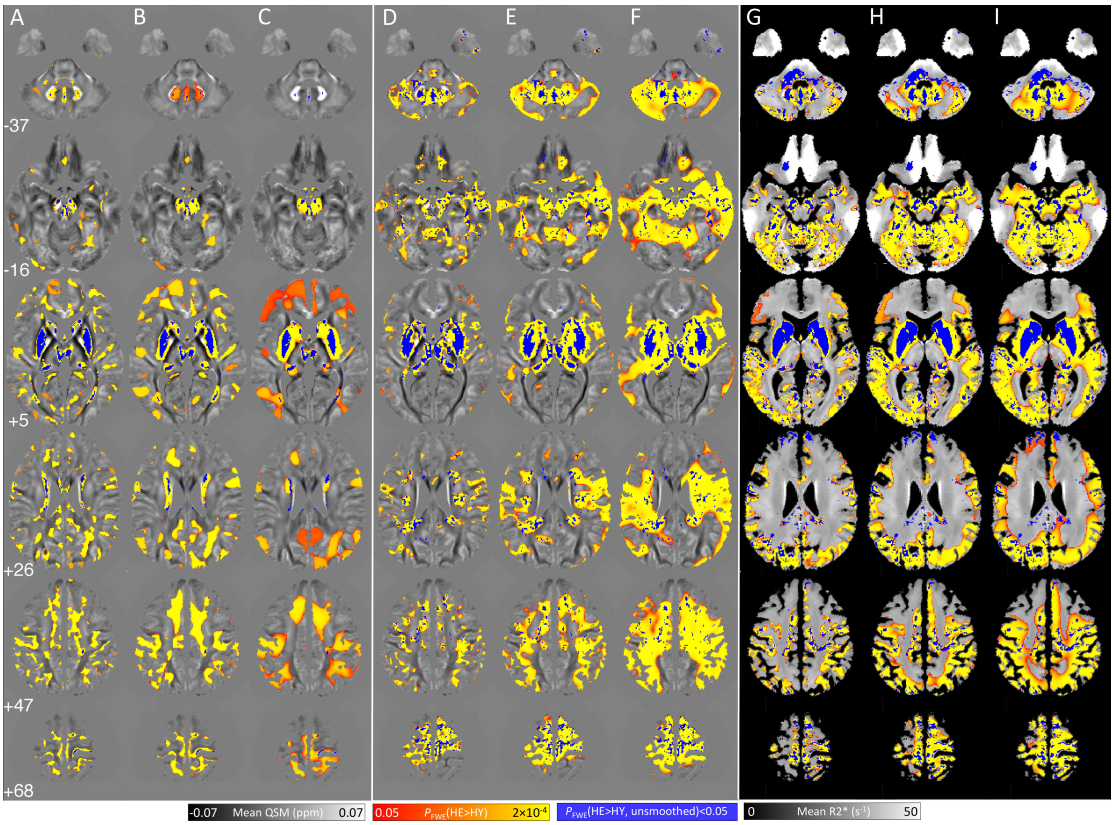

Figure 3. Impact of varying Gaussian smoothing kernel widths for (A-C) signed QSM, (D-F) absolute QSM and (G-I) R_2*. Blue clusters represent significant old versus young differences without smoothing. The left column for each metric (A, D and G) show smoothing-compensated results for a kernel with standard deviation (sigma) of 1.5 mm; middle columns (B, E and H) show significant clusters applying a 3-mm wide kernel; and (C, F and I) for 5-mm sigma. Abbreviations: healthy elderly (HE), healthy young (HY).

2.11 Impact of global atrophy on whole-brain analyses

Furthermore, it is unknown whether the impact of global brain atrophy (e.g. due to co-registration performance bias, which may play a role when contrasting old versus young subjects) could drive QSM/R_2* whole-brain results. We tested whether this could be true in two steps: (i) with a linear model on the null hypothesis that QSM/R_2*, for each group separately, do not interact with a global atrophy measure – estimated as total brain volume (sum of GM plus WM voxels with probability greater than 0.5) adjusted by a measure of intracranial volume

(Jack et al., 1989) determined using a previously validated method (Pengas et al., 2009); then if (i) cannot be rejected, (ii) with a second linear model formulated on the null hypothesis that QSM/R_2* group differences cannot be globally explained by adjusted brain volumes. Negative results (i.e. insufficient statistical significance to reject any of the two hypotheses) across the whole brain confirmed that with the proposed methodology age-related QSM/R_2* effects are largely independent of global atrophy.

2.12 QSM dependence on head orientation and sex

QSM estimations in a uniaxial environment such as WM are known to be orientation-dependent (Liu, 2010). We calculated the angle of the anterior commissure/posterior commissure line with respect to the axial plane perpendicular to the main magnetic field for each subject, and found a slight head angulation difference between groups (α_y=3.3±3.2°, α_e=7.0±5.0°; two-tailed Wilcoxon rank-sum test of equal medians: Z=-2.9, p=0.008). We, therefore, tested whether QSM data dispersion in older adults could be explained by systematic differences in head orientation by way of a two-group comparison using an analogous permutation-based framework as described in section 2.11, only in this instance, adding head orientation as a variable of interest to the design matrix. As with atrophy, we found no evidence supporting this prediction. It was concluded, therefore, that although it is important to continue challenging the impact of systematic differences in brain angulation, this would need to be large in absolute terms (>>5±5°) to induce a non-negligible QSM dependency.

Using the same strategy, only with sex as the variable of interest, we also tested whether whole-brain QSM/R2* effects in young and older adults were different between males and females but neither null hypothesis (sex interaction or main effect) could be rejected, which is consistent with our previous 3T results showing negligible effects in most subcortical structures (Acosta-Cabronero et al., 2016).

2.13 Regional QSM and R_2 analyses*

For ROI analyses, median values of unsmoothed signed QSM, absolute QSM and R_2* values were extracted bilaterally from the caudate nucleus, putamen, globus pallidus (GP), hippocampus, amygdala and thalamus automatically using the FIRST algorithm (Patenaude et al., 2011) on the anatomical T_1 template image. An additional six subcortical ROIs, namely the red nucleus (RN), subthalamic nucleus (STN), substantia nigra (SN), cerebellar dentate nucleus (DN) and internal (GPi) and external pallidum (GPe) were manually traced on the QSM template. In order to reduce edge effects, all deep brain ROIs were eroded in 3D by convolution with a 1-mm radius spherical kernel.

Median values were also calculated from cortical ROIs inferred from the Desikan-Killiany-Tourville (DKT) atlas (Klein and Tourville, 2012). The OASIS-30 template and OASIS-TRT-20 joint fusion atlas (in OASIS-30 space) were obtained

from Mindboggle's repository (http://www.mindboggle.info/data). The study-wise to OASIS-30 space nonlinear warp field was calculated with a deformable b-spline co-registration routine in ANTs ('antsRegistrationSyN'). DKT labels were brought into the study space using the inverse of such transformation and nearest-neighbour interpolation. Finally, to minimise partial-volume contamination and co-registration errors, each cortical ROI was intersected with a study-wise GM mask – the warped, population-average GM segment binarised at a probability cut-off of 0.5.

ROIs in WM were similarly inferred from Johns Hopkins' ICBM-DTI-81 WM atlas (Mori et al., 2008). Warped (to study space with ANTs) ROI labels were intersected by a population-average WM mask and the complement mask of all cortical and subcortical ROIs.

See Fig. 4 for summary of all selected regions.

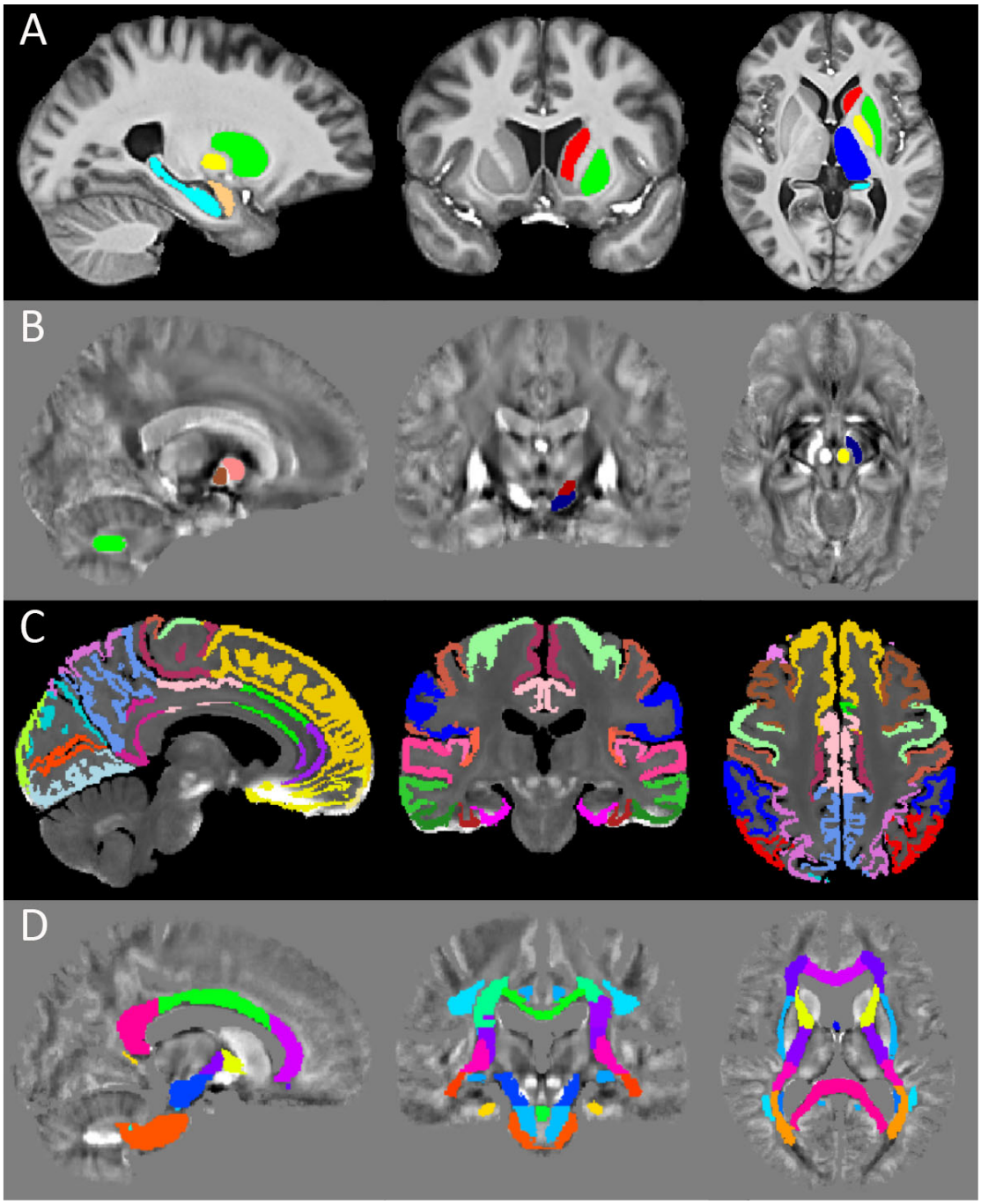

Figure 4. Summary of all segmented regions of interest. In panel (A) caudate nucleus (red), putamen (green), globus pallidus (GP; yellow) thalamus (blue), hippocampus (turquoise) and amygdala (copper) were segmented bilaterally from the anatomical T_1 template using FSL FIRST (Patenaude et al., 2011). In (B), the internal globus pallidus (GPi; brown), external globus pallidus (GPe; pink), dentate nucleus (DN; green) subthalamic nucleus (STN; red), substantia nigra (SN; blue) and red nucleus (yellow) were all segmented manually from the QSM template. In panel (C), example cortical ROIs inferred from the DKT atlas segmented from the study-wise T_1 template. In panel (D), example WM ROIs similarly inferred from the ICBM-DTI-81 white matter atlas.

2.14 Validity and reliability of template based extractions

In order to assess the validity of extracting quantitative information from small structural regions directly in template space, absolute QSM, signed QSM and R_2* data from each subject's native DN, RN, SN and STN were manually extracted and compared to those inferred from a single ROI traced in template space. Single-measure, intra-class correlation coefficients (ICC) +/- the 95% confidence interval (lower/upper bounds), taking the ROI as class and correlating across extraction methods, demonstrated overall that the proposed template based approach achieved high accuracy when compared to manually delineating ROIs in native space (see Table 1). The exceptions were DN, SN and STN extractions using signed and absolute QSM data, which were clearly influenced by their wide implicit data dispersion (see Table 2); in contrast, it must be noted R_2* extractions from DN and STN were in greater agreement.

For completeness, single-measure ICCs were also performed in regions segmented automatically using the FIRST algorithm. Taking the ROI as class and correlating across methods (T_1 native space vs template-based), ICC and 95% confidence intervals for caudate nucleus, putamen, GP, hippocampus, amygdala and thalamus using absolute QSM, signed QSM and R_2* values were generated (see Table 1). Overall, template derived values were in excellent agreement with native extractions using FIRST. Signed QSM values demonstrated the greatest variability, however absolute QSM and R_2* ICCs for all ROIs were highly concordant.

		DN	RN	SN	STN	Caud	Put	GP	Hippo	Amyg	Thal
ICC (95%)	**QSM signed**	0.58 (0.12-0.80)	0.96 (0.92-0.98)	0.64 (0.20-0.83)	0.38 (0.09-0.61)	0.98 (0.97-0.99)	0.99 (0.99-1.0)	0.71 (0.52-0.84)	0.93 (0.87-0.96)	0.84 (0.72-0.91)	0.89 (0.80-0.94)
	|QSM|	0.63 (0.14-0.83)	0.96 (0.91-0.98)	0.82 (0.68-0.90)	0.38 (0.09-0.61)	0.98 (0.97-0.99)	0.99 (0.99-0.99)	0.87 (0.76-0.93)	0.97 (0.94-0.98)	0.98 (0.96-0.99)	0.99 (0.98-1.0)
	R_2*	0.85 (0.73-0.92)	0.86 (0.75-0.92)	0.65 (0.43-0.80)	0.73 (0.55-0.85)	0.99 (0.97-1.0)	1.0	0.91 (0.83-0.95)	0.98 (0.97-0.99)	0.98 (0.95-0.99)	0.99 (0.99-1.0)

Table 1. Validity measures for template based ROI extractions. Single-measure ICC +/- the 95% confidence interval (lower/upper bounds), taking the ROI as class and correlating across methods (native vs template-derived values) for manual (displayed on left) and automatically (displayed on right) segmented ROIs. Abbreviations: region of interest (ROI), intra-class correlation coefficient (ICC), absolute QSM (|QSM|), red nucleus (RN), substantia nigra (SN), subthalamic nucleus (STN), caudate nucleus (Caud), putamen (Put), globus pallidus (GP), hippocampus (Hippo), thalamus (Thal), dentate nucleus (DN).

Test-retest reliability of absolute QSM, signed QSM and R_2* data extracted from SN, RN and DN ROIs traced by two different raters (M.B. and J.A-C.) was also evaluated using a single-measure ICC. For QSM extractions from SN, RN and DN, ICC +/- the 95% confidence interval, were 0.97 (0.95–0.99), 0.99 (0.99 – 1.00)

and 0.94 (0.89–0.97) respectively. For R_2*, SN, RN and DN extractions, ICC and 95% confidence were 0.99 (0.98–0.99), 0.98 (0.97 – 0.99) and 0.94 (0.88–0.97), respectively, demonstrating that the proposed template-based ROI extraction approach is highly reproducible.

2.15 Regional inter-hemispheric differences

Inter-hemispheric differences in absolute QSM, signed QSM and R_2* were probed using Wilcoxon rank-sum tests, which revealed that left/right measurements were consistent across the whole brain ($p>0.05$). In order to improve measurement stability, thus, median ROI values were averaged across hemispheres prior to computing old-versus-young Wilcoxon rank-sum statistics. In addition, to correct for the effect of multiple comparisons a statistical threshold of $p<0.004$ was set throughout (i.e. Bonferroni-corrected $p<0.05$ for 12 tests). All tests were performed two-tailed.

2.16 Effect-size calculation

Z' scores were computed to compare the sensitivity of QSM and R_2* measurements in each ROI. A Z' score—acting as a measure of effect size—was defined as the group mean difference relative to the global standard deviation:

$$Z' = \frac{\mu_e - \mu_y}{\sigma_y + \sigma_e}, \quad (1)$$

where μ_e represents the global mean across the elderly group, μ_y is the mean of the young control group, σ_e is the standard deviation across the elderly group and σ_y is the standard deviation across the young control group.

2.17 Computational framework

All data postprocessing was performed on a desktop computer with two, 3.1-GHz octa-core hyper-threading CPUs, 64 GB DDR3 RAM and four solid-state drives operated by Ubuntu Linux 12.04. All processing tasks (including QSM reconstruction and regional data extraction) unless stated otherwise were performed in the MATLAB environment (R2012a; The Mathworks Inc., Natick, MA, USA). Finally, ROI statistical tests were performed using the Statistical Package for the Social Sciences (SPSS), version 22.0.

3. RESULTS

3.1 Age-related differences in whole-brain QSM maps

Two-sample (elderly greater than young) permutation testing ($P_{FWE}<0.05$) on signed susceptibility maps (QSM) revealed significant age-related differences in several subcortical and cortical regions (Fig. 5). Within deep brain nuclei, extensive bilateral clusters were observed at the sites of the caudate nucleus and putamen (collectively referred to as the striatum), mesencephalon (RN and SN), diencephalon (STN, mammillary bodies and thalamus) and cerebellar DN. In

cortical GM, clusters of statistical significance were confluent and bilateral in superior frontal areas, namely the premotor cortex, primary motor cortex and supplementary motor area passing into the dorsal medial prefrontal cortex (PFC) and insula. More patchy alterations were observed in parietal cortices, lateral occipital areas, inferior frontal gyrus, ventral PFC and brainstem. Age-related QSM differences in WM were overall less extensive, although a large cluster was identified in posterior parietal WM at the site of the optic radiation. In all cases, non-normalised signed QSM values are presented throughout.

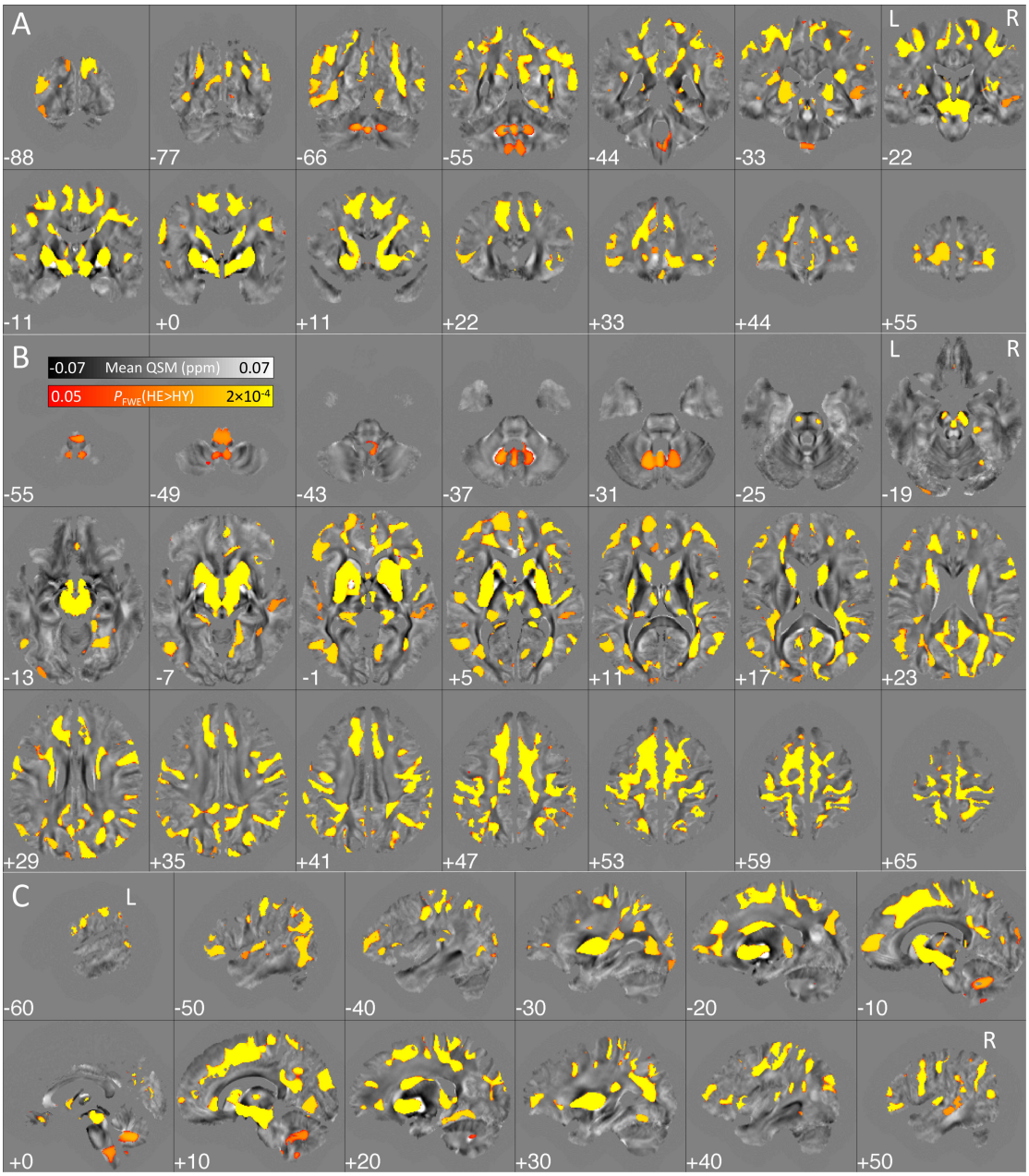

Figure 5. Whole-brain age-related distribution of increased signed QSM. Thresholded (P_{FWE}<0.05) statistical map for the cluster-wise comparison between N=20 older and N=20 younger adults using non-normalised QSM values. Results were standardized to MNI152 space and overlaid onto the MNI-

warped mean QSM template (N=40). Abbreviations: healthy elderly (HE), healthy young (HY).

The opposite contrast (i.e. signed QSM reductions in older adults) also revealed widespread alterations but mostly in WM (Fig. 6). Notably, large bilateral clusters were identified in internal and external capsule, corpus callosum, prefrontal, temporal, cerebellar and pontine WM. In several areas, however, significant clusters also extended across GM regions e.g. cingulate, thalamus, occipital and cerebellar cortex bilaterally.

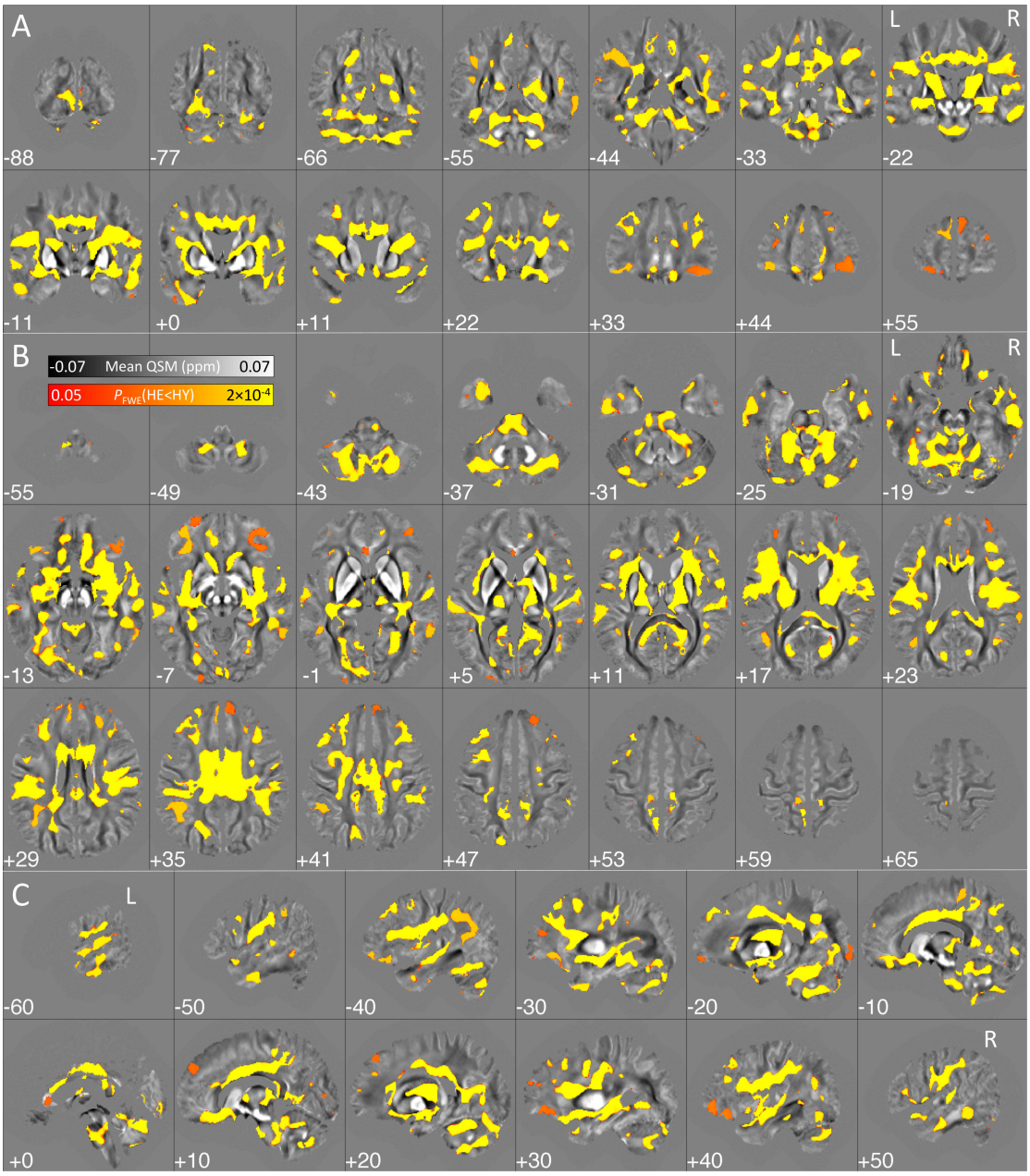

Figure 6. Whole-brain age-related distribution of signed QSM reductions. Thresholded (P_{FWE}<0.05) statistical map for the cluster-wise comparison between older and younger adults using non-normalised QSM values. Results were standardized to MNI152 space and overlaid onto the warped mean QSM

template. Abbreviations: healthy elderly (HE), healthy young (HY).

Fig. 7 illustrates the whole-brain results for increased positive-only QSM and reduced negative-only QSM in older adults, both of which are highly consistent with results from positive (increased in older adults) and negative (decreased) contrasts using signed QSM data (Fig. 5 and 6, respectively). Slightly differential effects, however, were observed for increased positive-QSM (relative to increased signed QSM), where more patchy behaviour was observed in ventral prefrontal and occipital areas, whereas more extensive clusters were identified in the right temporal lobe. The opposite contrasts (i.e. decreased positive-QSM and increased negative-QSM in older adults) did not reveal any statistically significant difference at the corrected threshold level used throughout the present study ($P_{FWE}<0.05$).

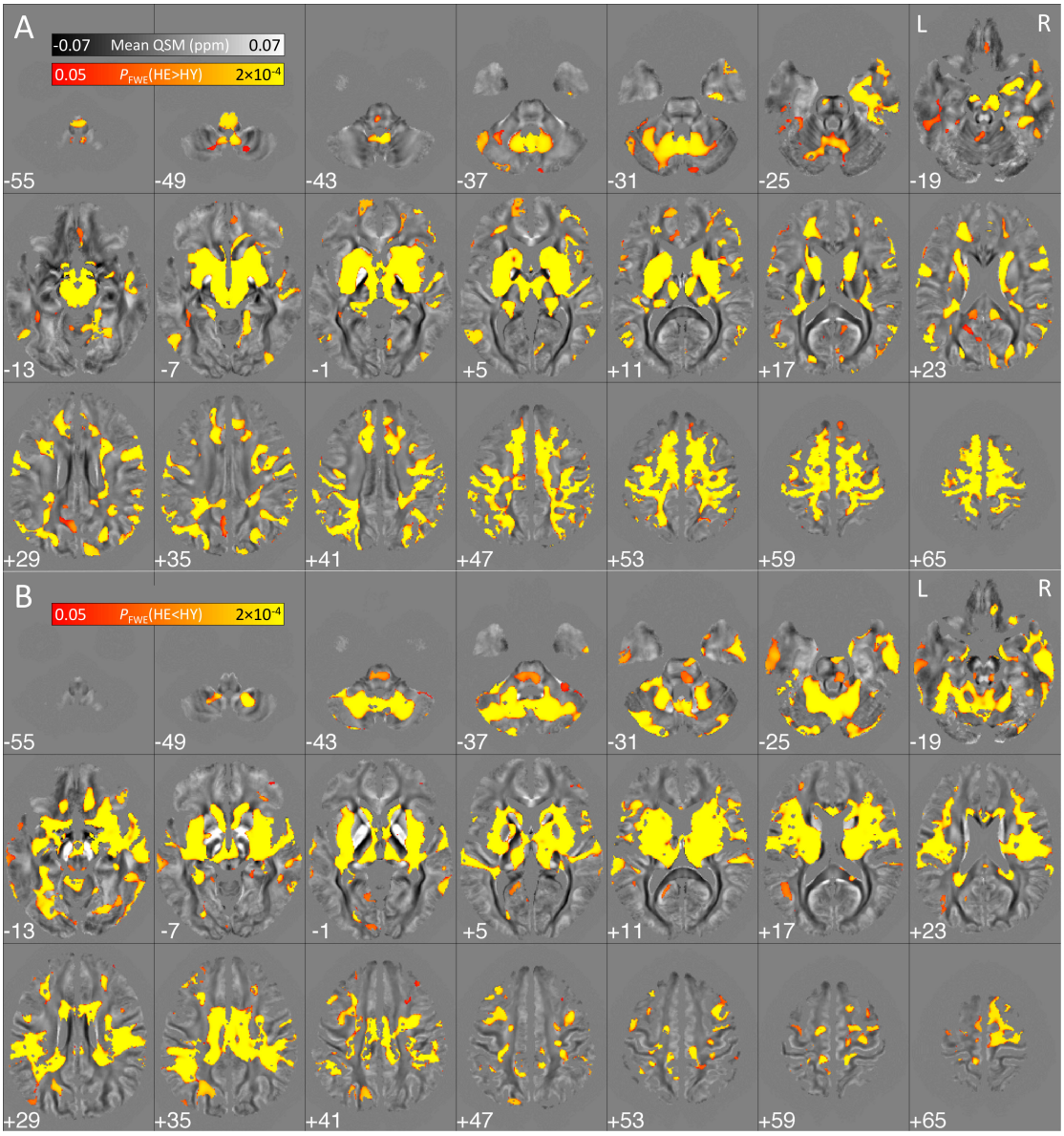

Figure 7. Whole-brain distribution of age-related (A) greater positive-only QSM

and (B) reduced negative-only QSM. Thresholded (P_{FWE}<0.05) statistical maps for the cluster-wise comparison between older and younger adults using non-normalised QSM values. Results were standardized to MNI152 space and overlaid onto the warped mean QSM template. Abbreviations: healthy elderly (HE), healthy young (HY).

Whole-brain results for increased absolute QSM in older adults—shown in Fig. 8—were also highly consistent with those for signed QSM. As a composite of positive and negative effects, however, clusters in Fig. 8 extended across subcortical structures and dorsal prefrontal, temporal and cerebellar areas, primarily in the cortex but also in WM. As with signed QSM, non-normalised absolute QSM values are presented throughout. Interestingly, results for absolute QSM were also less extensive in ventral prefrontal, inferior parietal and occipital areas than increased signed QSM in older adults; whereas stronger effects were observed in right temporal areas including hippocampus and amygdala. The opposite contrast (i.e. age-related decreases in absolute QSM) did not return any statistically significant difference.

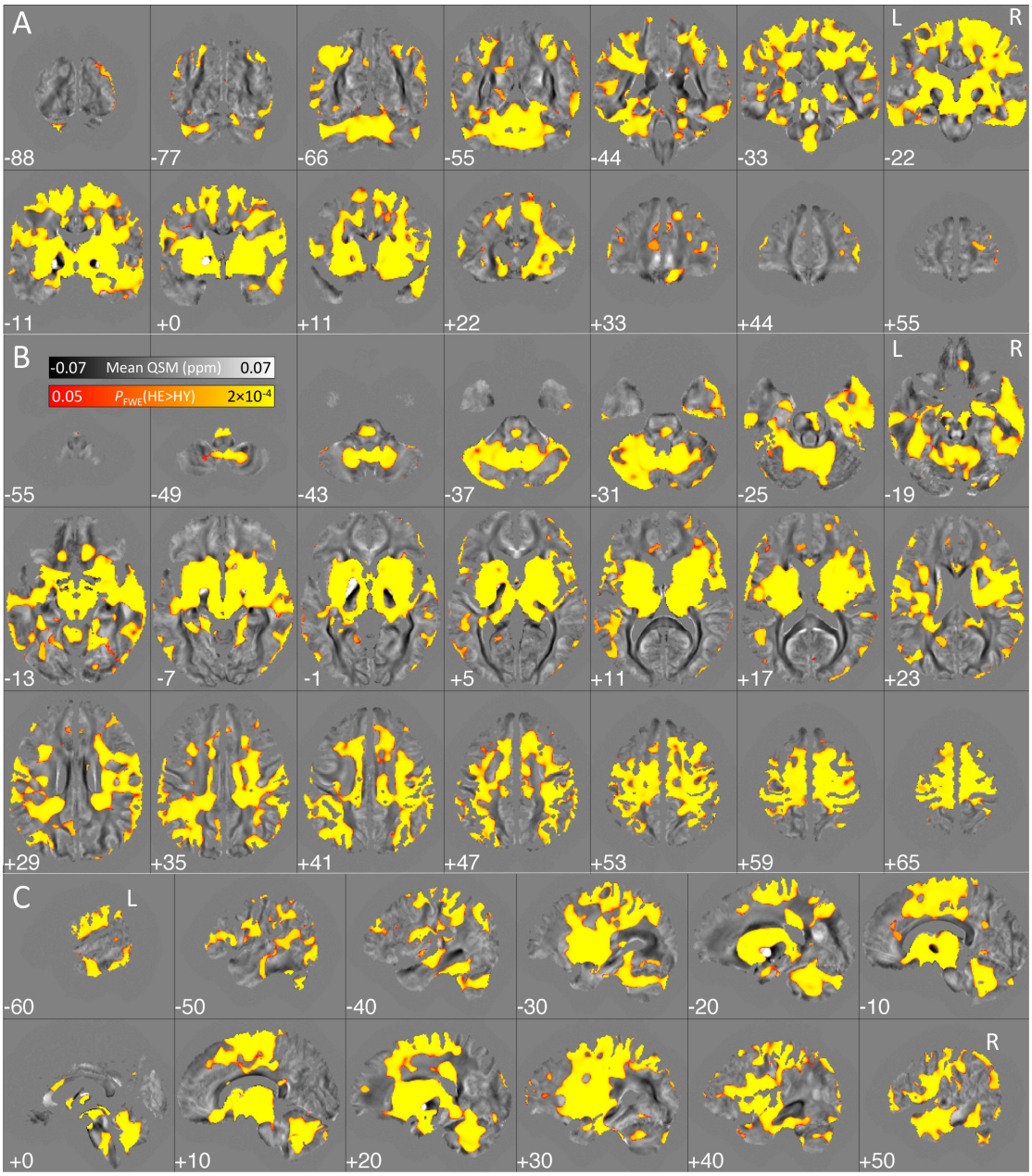

Figure 8. Whole-brain distribution of age-related increases in absolute QSM. Thresholded (P_{FWE}<0.05) statistical map for the cluster-wise comparison between older and younger adults using non-normalised QSM values. Results were standardized to MNI152 space and overlaid onto the warped mean QSM template. Abbreviations: healthy elderly (HE), healthy young (HY).

3.2 Age-related differences in whole-brain R_2 maps*

R_2* thresholded (P_{FWE}<0.05) statistical maps (elderly greater than young) also revealed strong age-related differences in many cortical and subcortical regions (Fig. 9). Within deep brain nuclei, confluent bilateral distributions were observed in the striatum, GP, midbrain, STN, medulla oblongata and DN. Predominantly unilateral effects were also observed in the right amygdala and

hippocampus. No such effects were observed in the thalamus, with the exception of the pulvinar. In the cortex, confluent and bilateral R_2* increases were observed in occipital, parietal, temporal, superior prefrontal, insular (predominantly posterior) and cerebellar regions. In contrast to the QSM distribution, age-related differences were chiefly restricted to GM. The opposite contrast (i.e. age-related R_2* reduction) was completely negative.

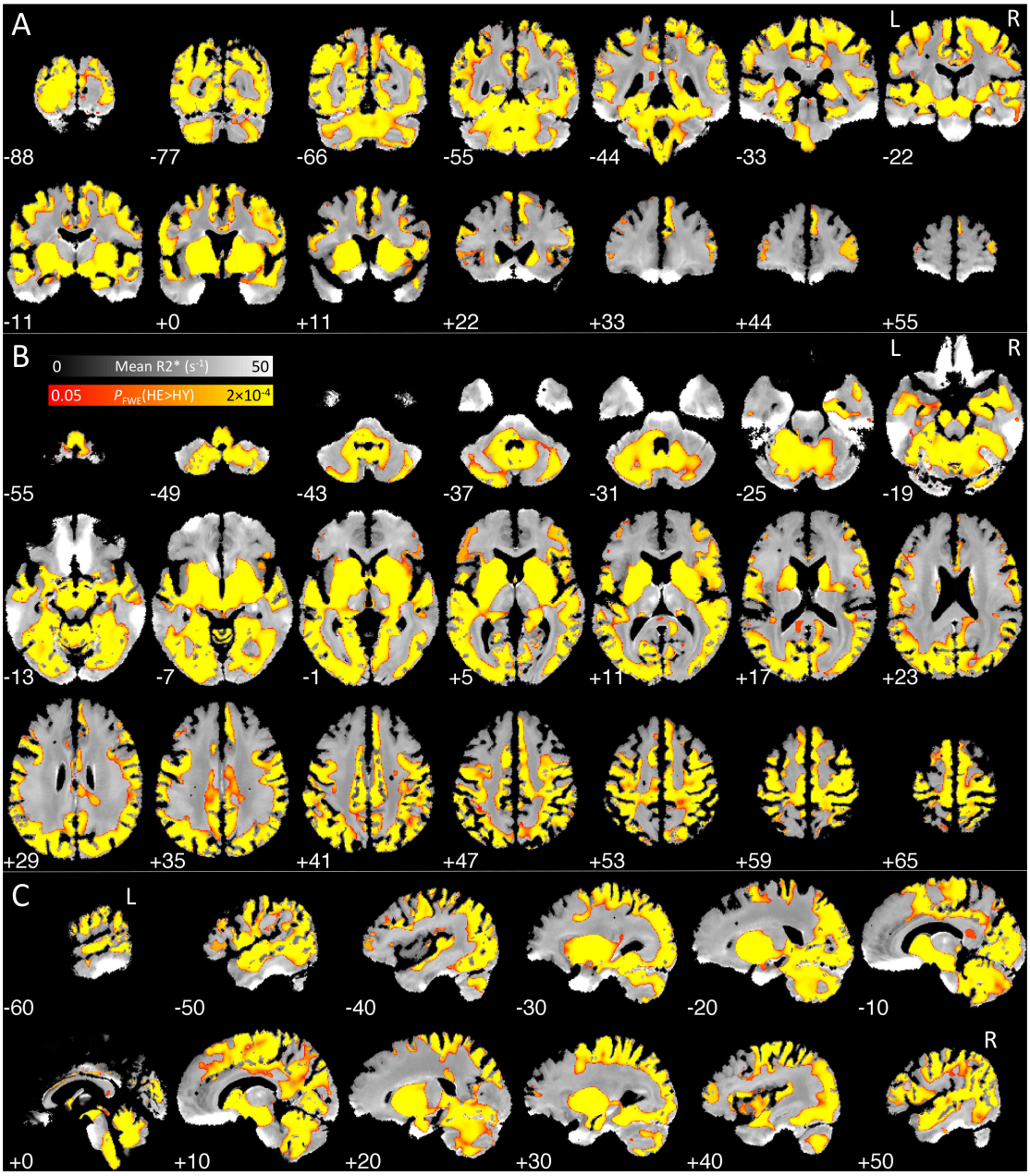

Figure 9. Whole-brain distribution of age-related increases in R_2*. Thresholded (P_{FWE}<0.05) statistical map for the cluster-enhanced comparison between older and younger adults. Results were standardized to MNI152 space and overlaid onto the warped mean R_2* template. Abbreviations: healthy elderly (HE), healthy young (HY).

*3.3 Deep brain regional analysis using QSM and R_2**

The deep brain ROI analysis confirmed significant age-related absolute QSM increases in the RN, caudate nucleus, putamen and thalamus (Fig. 10A; rank-sum tests all $p<0.0001$), SN and hippocampus ($p<0.001$), STN and DN (both $p<0.05$, Bonferroni-corrected for 12 tests). An age-related increase was also observed in the amygdala but it did not survive Bonferroni correction. No significant effects were observed in the GP, or its GPi and GPe sub-regions (see Table 2).

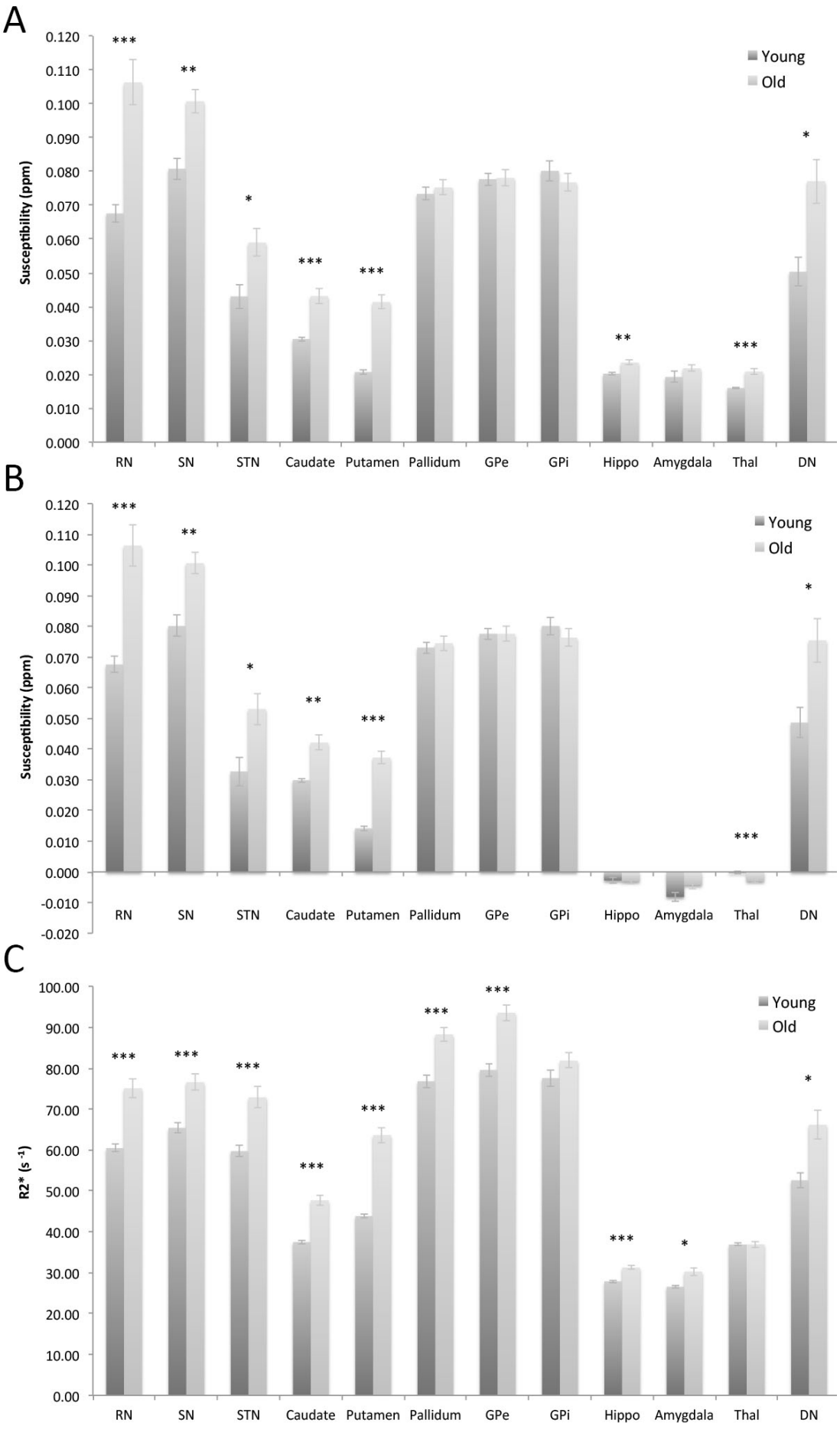
A
Susceptibility (ppm)
0.120
0.110
0.100
0.090
0.080
0.070
0.060
0.050
0.040
0.030
0.020
0.010
0.000
Young
Old
***
**
*
***
***
**
***
*
RN
SN
STN
Caudate
Putamen
Pallidum
GPe
GPi
Hippo
Amygdala
Thal
DN
B
Susceptibility (ppm)
0.120
0.110
0.100
0.090
0.080
0.070
0.060
0.050
0.040
0.030
0.020
0.010
0.000
-0.010
-0.020
Young
Old
***
**
*
**
***
***
*
RN
SN
STN
Caudate
Putamen
Pallidum
GPe
GPi
Hippo
Amygdala
Thal
DN
C
R2* (s -1)
100.00
90.00
80.00
70.00
60.00
50.00
40.00
30.00
20.00
10.00
0.00
Young
Old
***
***
***
***
***
***
***
***
*
*
RN
SN
STN
Caudate
Putamen
Pallidum
GPe
GPi
Hippo
Amygdala
Thal
DN

Figure 10. Regional summary statistics for subcortical ROIs. (A) Mean ± S.E.M for absolute susceptibility maps (in parts per million), (B) for signed susceptibility (ppm), and (C) for R_2* (s^{-1}) in major deep brain nuclei of young and older adults. Non-normalised QSM values are reported throughout. Abbreviations: red nucleus (RN), substantia nigra (SN), subthalamic nucleus (STN), external globus pallidus (GPe), internal globus pallidus (GPi), hippocampus (Hippo), thalamus (Thal), dentate nucleus (DN). *** ($p<0.0001$), ** ($p<0.001$), * ($p<0.004$; Bonferroni-corrected $p<0.05$ for 12 tests), indicate significant difference in old compared to younger adults (Wilcoxon ranked-sum tests).

For signed QSM values, significant age-related differences in the RN, putamen, thalamus (Fig. 10B; rank-sum tests all $p<0.0001$), SN, caudate ($p<0.001$), STN and DN (both $p<0.05$, Bonferroni-corrected for 12 tests) were observed in older adults.

The R_2* ROI analysis found significant age-related increases in the RN, SN, STN, caudate nucleus, putamen, GP localized to the external segment (GPe), hippocampus (all $p<0.0001$), amygdala and DN ($p<0.05$, Bonferroni-corrected for 12 tests). No significant effects were observed in the GPi and thalamus (Fig. 10C; Table 2). Furthermore, male-versus-female group comparisons for both QSM and R_2* values were negative in all deep brain regions of interest (rank-sum test; $p>0.05$; Bonferroni-corrected for 12 tests).

Significant effect-size differences (absolute QSM > signed QSM) were identified (Wilcoxon signed-ranks test; $p<0.05$, Bonferroni-corrected for 12 tests) in RN, SN, caudate, putamen, hippocampus thalamus and DN (all $p < 0.001$, see Table 2). More generally, in all ROIs (except for the amygdala), absolute QSM returned both enhanced age-related differences and reduced relative variance (as would be expected from taking the absolute to a set of real numbers). Comparing absolute QSM with R_2* Z' scores also revealed a significant increase in sensitivity to age-related differences for absolute QSM in the thalamus and for R_2* in the GP (both in GPe and GPi).

			RN	SN	STN	Caud	Put	GP	GPe	GPi	Hippo	Amyg	Thal	DN
Group Stats	**Mean QSM signed ± SEM (ppm)**	**HY**	0.068 ± 0.0025	0.080 ± 0.0035	0.033 ± 0.0047	0.030 ± 0.0007	0.014 ± 0.0008	0.073 ± 0.0018	0.078 ± 0.0018	0.080 ± 0.0030	-0.003 ± 0.0009	-0.008 ± 0.0016	-0.0002 ± 0.0004	0.049 ± 0.0048
		HE	0.106 ± 0.0067	0.101 ± 0.0035	0.053 ± 0.0012	0.042 ± 0.0023	0.037 ± 0.0022	0.075 ± 0.0024	0.078 ± 0.0024	0.076 ± 0.0029	-0.003 ± 0.0009	-0.004 ± 0.0012	0.003 ± 0.0005	0.075 ± 0.0071
	Rank-sum test	**Z**	-3.9	-3.5	-2.8	-3.5	-5.4	NA	NA	NA	NA	NA	-3.7	-3.0
		P	**<0.0001**	**0.0003**	**0.004**	**0.0003**	**<0.0001**	0.4	0.7	0.5	0.6	0.2	**<0.0001**	**0.002**
	Mean |QSM| ± SEM (ppm)	**HY**	0.068 ± 0.0025	0.081 ± 0.0031	0.043 ± 0.0036	0.031 ± 0.0006	0.021 ± 0.0007	0.073 ± 0.0018	0.078 ± 0.0018	0.080 ± 0.0030	0.020 ± 0.0005	0.019 ± 0.0015	0.016 ± 0.0003	0.050 ± 0.0042
		HE	0.106 ± 0.0067	0.101 ± 0.0034	0.059 ± 0.0041	0.043 ± 0.0022	0.041 ± 0.0021	0.075 ± 0.0022	0.078 ± 0.0023	0.078 ± 0.0027	0.024 ± 0.0006	0.022 ± 0.0010	0.021 ± 0.0008	0.077 ± 0.0065
	Rank-sum test	**Z**	-3.9	-3.5	-2.9	-3.9	-5.4	NA	NA	NA	-3.4	NA	-4.2	-3.2
		P	**<0.0001**	**0.0002**	**0.004**	**<0.0001**	**<0.0001**	0.3	0.5	0.5	**0.001**	0.05	**<0.0001**	**0.001**
	Mean R_2* ± SEM (s^{-1})	**HY**	60 ± 0.90	65 ± 1.3	60 ± 1.5	37 ± 0.45	44 ± 0.56	77 ± 1.6	80 ± 1.6	78 ± 2.0	28 ± 0.35	27 ± 0.44	37 ± 0.34	53 ± 1.8

		HE	75 ± 2.3	77 ± 1.9	73 ± 2.5	48 ± 1.2	64 ± 1.9	88 ± 1.8	94 ± 2.0	82 ± 1.8	31 ± 0.50	30 ± 1.01	37 ± 0.75	66 ± 3.5
	Rank-sum test	**Z**	-4.5	-4.0	-4.3	-5.3	-5.4	-4.1	-4.3	NA	-4.4	-3.2	NA	-3.1
		P	**<0.0001**	**0.0002**	**0.0001**	**<0.0001**	**<0.0001**	**0.0002**	**<0.0001**	0.06	**0.0001**	**0.001**	0.6	**0.002**
	Z'-score (HE vs HY effect size)	**|QSM|**	0.94++	0.68++	0.47	0.98++	1.7++	0.11	0.02	-0.14	0.64++	0.23	0.95++	0.56++
		QSM signed	0.89	0.65	0.46	0.90	1.5	0.08	0.01	-0.15	-0.05	0.30	-0.69	0.50
		QSM Norm	0.77	0.55	0.35	0.94	1.4	0.03	-0.09	-0.05	0.31	0.47	0.34	0.54
		R_2*	1.0	0.77	0.74	1.4	1.8	0.76	0.88	0.25	0.88	0.57	0.007	0.58
|QSM| vs R_2*	**Signed-ranks test**	**Z**	NA	NA	NA	NA	NA	-3.4	-3.6	-2.9	NA	NA	-3.7	NA
		P	0.9	0.8	0.06	0.04	0.7	**0.001**	**<0.0001**	**0.004**	0.04	0.006	**<0.0001**	1.0

Table 2. Summary of regional group statistics. Abbreviations: healthy young (HY), healthy elderly (HE), red nucleus (RN), substantia nigra (SN), subthalamic nucleus (STN), caudate nucleus (Caud), putamen (Put), globus pallidus (GP), external globus pallidus (GPe), internal globus pallidus (GPi), hippocampus (Hippo), thalamus (Thal), dentate nucleus (DN), absolute QSM (|QSM|), normalised QSM (norm), not significant (NS), not applicable (NA). ++ Significant differences between absolute and signed-QSM Z' scores ($p<0.001$, post-hoc Wilcoxon ranked-sum tests).

*3.4 Cortical regional analysis using QSM and R_2**

The cortical ROI analysis confirmed significant age-related absolute QSM differences in fusiform (Fus), paracentral (PC), pars opercularis (POPE), postcentral (POC), posterior cingulate (PCC), precentral (PREC), superior frontal (SFC), superior temporal (STC), supramarginal (SMC) and insula (Ins) (Fig. 11A; rank-sum tests all $p<0.0001$), caudal middle frontal (CMF) and superior parietal cortex (SPC) (both $p<0.001$). Using signed QSM values, significant age-related differences were observed in triangularis (PTRI) and PCC (Fig. 11B; rank-sum tests both $p<0.0001$), PC and transverse temporal cortex (TTC) (both $p<0.001$). For R_2*, extensive significant age-related differences in the cortex were observed in cuneus (Cun), Fus, inferior parietal (IPC), lateral occipital (LOC), lingual (Ling), middle temporal (MTC), parahippocampal (PHC), PC, pars orbitalis (POPE), PTRI, pericalcarine (PCAL), postcentral (POC), PCC, PREC, precuneus (PCUN), SPC, STC and TTC (Fig. 11C; rank-sum tests all $p<0.0001$), anterior cingulate ACa, caudal middle frontal (CMF), isthmus cingulate (ISTC), rostral middle frontal (RMFC), SFC, SMC and Ins (all $p<0.001$).

Significant effect-size differences (absolute QSM > signed QSM) were identified in PCC and PREC (Wilcoxon signed-ranks test; $p<0.0001$), Fus, POPE, POC, STC and Ins (all $p<0.001$), ITC and LOC ($p<0.05$, Bonferroni-corrected for 31 tests) demonstrating absolute QSM also returned greater age-related differences in the cortex. Comparing absolute QSM and R_2* Z' scores revealed a significant increase in sensitivity to age-related differences for absolute QSM in Ins. In contrast R_2* demonstrated superior sensitivity in detecting age-related differences in Ling

and PCAL. Overall absolute QSM and R_2* Z' scores revealed highly comparable effect sizes in the cortex although significant differences in effect sizes (those for R_2* greater than for absolute QSM) were found in Ling, PCAL and Ins.

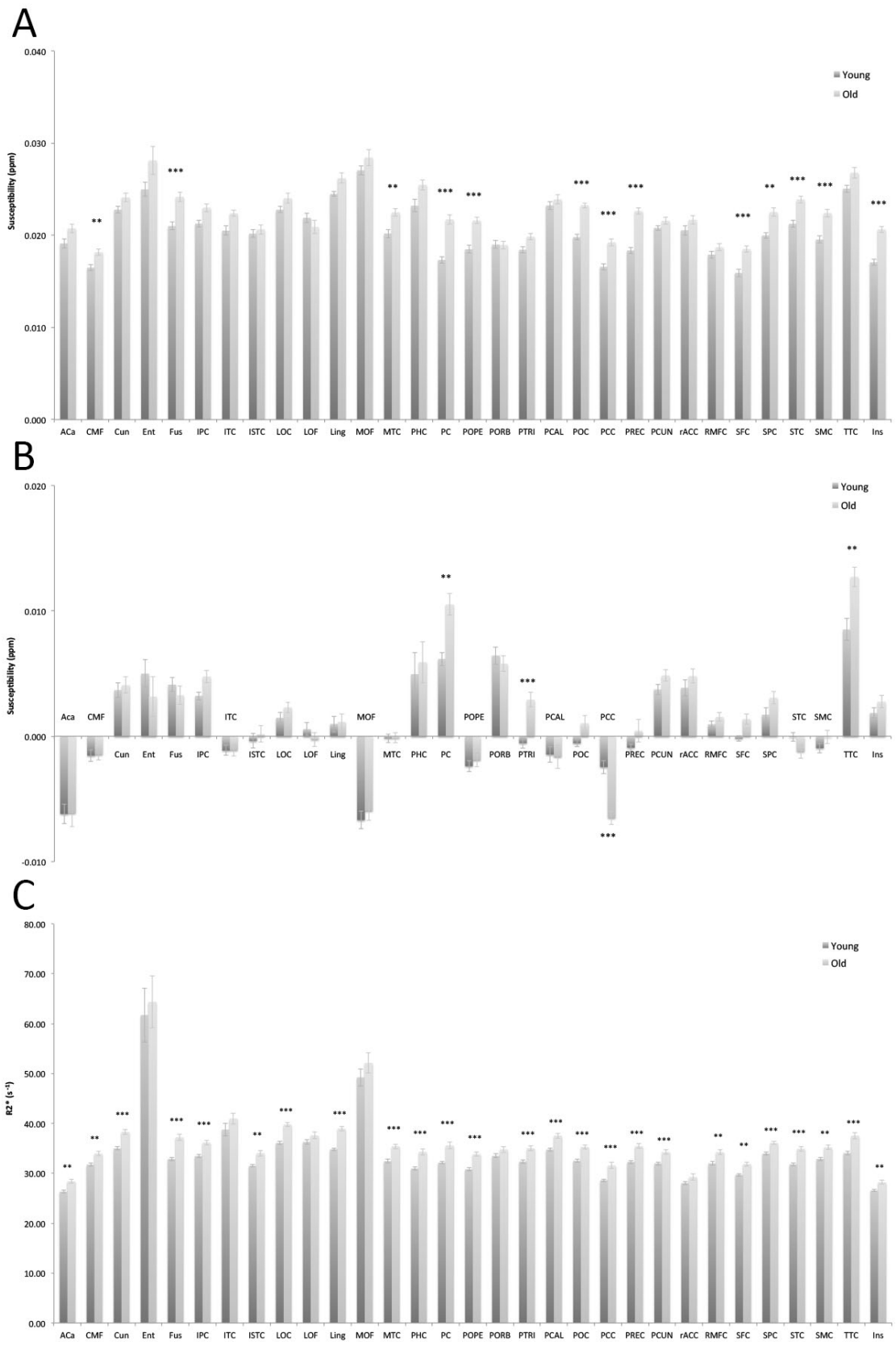

Figure 11. Regional summary statistics for cortical ROIs. (A) Mean ± S.E.M for absolute susceptibility maps (in parts per million), (B) for signed susceptibility (ppm), and (C) for R_2* (s^{-1}) in cortical regions of young and older adults. Non-normalised QSM values are reported throughout. Abbreviations: caudal anterior cingulate (ACa), caudal middle frontal (CMF), cuneus (CUN), entorhinal (ENT), fusiform (Fus), inferior parietal (IPC), inferior temporal cortex (ITC), isthmus cingulate (ISTC), lateral occipital (LOC), lateral orbitofrontal (LOF), lingual (Ling), medial orbitofrontal (MOF), middle temporal (MTC), parahippocampal (PHC), paracentral (PC), pars opercularis (POPE), pars orbitalis (PORB), triangularis (PTRI), pericalcarine (PCAL), postcentral (POC), posterior cingulate (PCC), precentral (PREC), precuneus (PCUN), rostral anterior cingulate (rACC), rostral middle frontal (RMFC), superior frontal (SFC), superior parietal (SPC), superior temporal (STC), supramarginal (SMC), transverse temporal (TTC), insula (Ins). *** ($p<0.0001$), ** ($p<0.001$) indicate significant difference in old compared to younger adults (Wilcoxon ranked-sum tests).

*3.5 White matter regional analysis using QSM and R_2**

The WM ROI analysis confirmed significant age-related absolute QSM differences in anterior limb of internal capsule (ALIC), posterior limb of the interior capsule (PLIC), posterior thalamic radiation (PTR) and superior longitudinal fasciculus (SLF) (Fig. 12A; rank-sum tests all $p<0.0001$), superior corona radiate (SCR) and external capsule (EC) (both $p<0.001$), body of corpus callosum (CC-B) and fornix (cres)/stria terminalis (FX/ST) ($p<0.002$; Bonferroni-corrected $p<0.05$ for 26 tests). Using signed QSM values, significant age-related differences were observed in ALIC, PLIC, PTR, superior fronto-occipital fasciculus (FOF) and tapetum (TAP) (Fig. 12B; rank-sum tests all $p<0.0001$), CC-B ($p<0.001$), SLF (Bonferroni-corrected $p<0.05$). For R_2*, significant age-related differences were observed in fornix (Fx-B) (Fig. 12C; rank-sum tests; $p<0.0001$), middle cerebellar peduncle (MCP) ($p<0.001$) and cerebral peduncle (CP) (Bonferroni-corrected $p<0.05$).

Significant effect-size differences (signed QSM vs absolute QSM) were identified in ALIC and SLF (Wilcoxon signed-ranks test; $p<0.0001$), CC-B, PLIC, PTR, EC, FX/ST, FOF (all $p<0.001$) and SCR (Bonferroni-corrected $p<0.05$). Comparing signed QSM with R_2* Z' scores revealed a significant increase in sensitivity to age-related differences for signed QSM in MCP, CC-B, splenium of corpus callosum (CC-Sp), inferior cerebellar peduncle (ICP), CP, ALIC, PLIC, anterior corona radiata (ACR), posterior thalamic radiation (PTR), FX/ST, SLF, FOF and TAP. On the contrary, QSM absolute and R_2* Z' scores in general were highly comparable although significant differences in effect sizes were found in FX-B, PLIC, SLF and TAP. Overall, however, these findings demonstrate age-related differences in WM are greater with signed QSM.

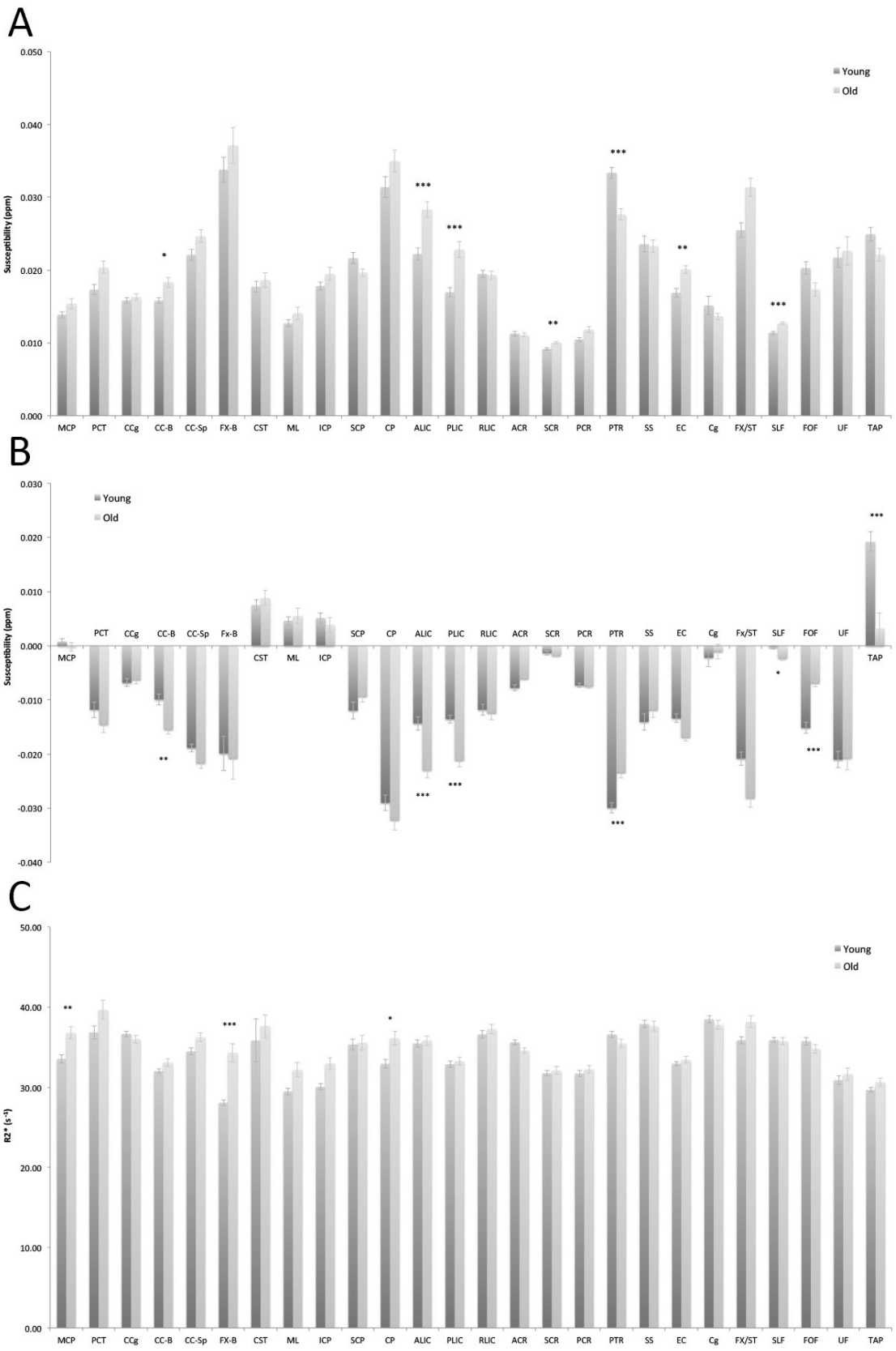

Figure 12. Regional summary statistics for WM ROIs. (A) Mean ± S.E.M for absolute susceptibility maps (in parts per million), (B) for signed susceptibility (ppm), and (C) for R_2* (s^{-1}) in WM regions of young and older adults. Non-normalised QSM values are reported throughout. Abbreviations: middle

cerebellar peduncle (MCP), pontine crossing tract (PCT), genu of corpus callosum (CCg), body corpus callosum (CC-B), splenium of corpus callosum (CC-Sp), fornix (Fx-B), corticospinal tract (CST), medial lemniscus (ML), inferior cerebellar peduncle (ICP), superior cerebellar peduncle (SCP), cerebral peduncle (CP), anterior limb of internal capsule (ALIC), posterior limb of internal capsule (PLIC), retrolenticular part of internal capsule (RLIC), anterior corona radiata (ACR), superior corona radiata (SCR), posterior corona radiata (PCR), posterior thalamic radiation (PTR), sagittal stratum (SS), external capsule (EC), cingulum (Cg), fornix (cres)/stria terminalis (FX/ST), superior longitudinal fasciculus (SLF), superior fronto-occipital fasciculus (FOF), uncinate fasciculus (UF), tapetum (TAP). *** ($p<0.0001$), ** ($p<0.001$), * ($p<0.002$; Bonferroni-corrected $p<0.05$ for 26 tests), indicate significant difference in old compared to younger adults (Wilcoxon ranked-sum tests).

4. DISCUSSION

This in vivo 7T MRI study demonstrated a novel application using whole brain methods to characterise the human aging process using both QSM and R_2* measurements. This is the first account to our knowledge to directly compare intra-subject QSM sensitivity with respect to R_2* using the same multi-GRE sequence. QSM revealed strong bilateral age-related differences (increased QSM values in older adults) in deep brain nuclei, namely putamen, caudate nucleus, thalamus, STN, RN, SN, hippocampus and DN. Age-related QSM alterations were also present in the cortex, particularly in superior motor areas, lateral parietal, insular, superior temporal and cerebellar cortices. Furthermore, WM differences—generally age-related QSM reductions but also an increase at the site of the posterior thalamic radiation—were also identified. Importantly, we found that age-related differences in R_2* measurements were more apparent than with QSM in GM in a distribution that also included the GP and most of the occipital cortex. In WM, R_2* abnormalities were restricted to the fornix and midbrain peduncles; thus, they were less widespread than QSM alterations.

In this study, we have proposed an additional magnetic susceptibility metric for the study of brain mineralisation, namely absolute QSM. This metric couples both (i) increases in positive-valued QSM and (ii) negative-valued QSM reductions in a single coherent effect; that is, aggregating non-local contributions from metal (e.g. paramagnetic iron) and alkaline/lipid species (e.g. diamagnetic calcium or myelin) into a single measure. It may seem counterintuitive to conglomerate two distinguishable effects into one measurement, but the practical benefits are relevant in that overall, absolute QSM improves statistical conditioning. This must be contextualised in a scenario where registration algorithms are imperfect, that such imperfections are more marked in the cortex due to its complex topology with some cortical areas being more prone to registration errors than others (Pereira et al., 2010). If, in such a scenario, the data type being warped (i.e. signed QSM) is also highly volatile, i.e. changing sign at a high spatial frequency, both factors, together, may result in unphysical high variances (Fig. 1) – a detrimental effect for quantitative analyses. In addition, in ROIs showing complex mineralization (e.g. simultaneous brain iron accumulation and calcification) or heterogeneous composition (e.g. susceptibility in some

subregions dominated by lipid-rich myelin and by iron-rich cells in another), absolute QSM can partly compensate for the counteracting effect in regional statistics of opposing susceptibility behaviours, thus, it can return greater effect sizes (Fig. 10 and Table 2); this might be crucial for the study of brain diseases where it might be desirable to identify an effect first, then explore the possible origins of such phenomenon.

Another general observation on signed QSM is that, with few exceptions, areas presenting an age-related increase in QSM (Fig. 5) stem from paramagnetic (QSM>0) behaviours (Fig. 7A), whereas the opposite behaviour (decreased QSM, Fig. 9) appears to emanate from predominantly diamagnetic (QSM<0) tissue such as WM (Fig. 7B). Generally, it could be argued that the latter might be a consequence of the former due to blooming or streaking artefacts spuriously rendering negative QSM values increasingly negative; however, we cannot yet rule out that some effects might be real. Future investigations—with ever-improving QSM inversion strategies—might shed light into this poorly understood behaviour. Until then, studying in combination both tails of the signed QSM distribution and the absolute value appears to be helpful to capture the full extent of QSM-derived effects.

It is noteworthy that the regional QSM results in deep brain nuclei were strongly concordant with the whole-brain analysis in that RN, SN, putamen, caudate nucleus, thalamus, STN, hippocampus and DN (in decreasing order of significance) demonstrated the strongest age-related differences (Fig. 10 and Table 2), which are consistent with previous *in vivo* MRI (Daugherty and Raz, 2013; Li et al., 2014; Poynton et al., 2015; Rodrigue et al., 2013; Acosta-Cabronero et al. 2016) and *post-mortem* iron analyses (Hallgren and Sourander, 1958; Ramos et al., 2014). Furthermore, the findings presented here also agree with the aforementioned studies in that independent of age, the basal ganglia system, RN and cerebellar DN contain more iron than the thalamus, hippocampus, amygdala, isocortex and WM.

The age-related differences reported with QSM in deep brain nuclei such as putamen, caudate, STN, SN, RN, hippocampus and DN were in the main highly concordant with R_2*. The striking exception to this agreement was an apparent age-related R_2* increase in the GP, which was found to be exclusively restricted to the external segment (GPe, Fig 4 and Table 2). In contrast, the GP result with QSM, whilst rich in iron in absolute terms, did not demonstrate an age-related increase. The high R_2* values for the GP (independent of age) in contrast to thalamus, caudate and putamen are consistent with previous *in vivo* R_2* reports and *post-mortem* correlations with iron concentration (Gelman et al., 1999; Langkammer et al., 2010; Péran et al., 2009; Yao et al., 2009). Furthermore, age-related increase in R_2* have been reported previously in the GP in some studies (Callaghan et al., 2014; Draganski et al., 2011). On the other hand, the lack of a significant age-related difference in the GP with QSM in the present study is consistent with previous *post-mortem* evidence (Hallgren and Sourander, 1958), and confirmed *in vivo* (Li et al., 2014), that iron deposition in the GP increases rapidly from birth until the second decade of life but thereafter plateaus. One study, however, reported age-related differences in the GPe—but not GPi—with

QSM (Ide et al., 2015). Overall, the differential GP behaviours in the present study are reflected in the existing literature, indeed a meta-analysis of past studies using various MR techniques to estimate iron content (Daugherty and Raz, 2013) concluded that the GP showed the weakest and most inconsistent age-related differences compared to other basal ganglia structures. One possibility for such inconsistency in past studies, could have been the presence of pre-clinical neurodegenerative diseases in older subjects, but this cannot explain the present discrepancy between R_2* and QSM which were derived from precisely the same cohort. If it were the case that the R_2* GPe increase in the present study were not spurious, one possible explanation for the absence of QSM effects could be that age-related pallidal micro-calcifications may cancel out increased paramagnetism driven by iron accumulation. Owing to its diamagnetic properties, calcium deposition may attenuate intra-voxel, age-related QSM increases due to its negative effect on total susceptibility. Whether it is plausible that pallidal calcification affects only the GPe and not GPi is another matter, but it is at least theoretically possible. All of these scenarios are, of course, only speculations at present; the key conclusion from this result is that age-related differences pertaining to iron concentration in the GP should be interpreted with extreme caution until more information is available, particularly from studies with *ex vivo* verification across the adult lifespan.

It is also known that QSM and R_2* are affected by myelin density variations in contrasting ways (Li et al., 2012; Liu, 2010; Liu et al., 2011; Schweser et al., 2011), chiefly modulated by myelin lipid/iron interactions (Fukunaga et al., 2010). It is noteworthy that the amount of myelin varies substantially in areas with high iron concentration as indicated by myelin stains (Schaltenbrand et al., 1977; Deistung et al., 2013), magnetisation transfer (MT; reflecting loss of macromolecular content) (Anik et al., 2007) and proton-induced X-ray emission (PIXE) maps (Stüber et al., 2014). In this scenario the presence of myelin may also locally attenuate susceptibility values, thus, it is plausible that in such regions, QSM may underestimate the true impact of iron accumulation. In contrast, tissue myelination in R_2* maps would lead to overestimated values of iron content (Deistung et al., 2013). A recent study using MT in aging identified a significant age-related decrease in the thalamus indicative of a reduction in macromolecular content – typically myelin (Callaghan et al., 2014). Furthermore, the substantial age-related differences reported here in WM with signed QSM namely in the corpus callosum and posterior thalamic radiation are also consistent with whole-brain decreases in MT reported by Callaghan et al., 2014, which may further point towards age-related differences in demyelination. This may explain the present findings in that although both R_2* and QSM found strong age-related increases in most subcortical structures beyond the mesencephalon, QSM values were overall lower than those in the SN. For instance, using R_2*, the STN exhibited similar values to SN and RN, whereas with QSM, even absolute values were relatively attenuated (Fig. 10). It could be, therefore, that in the STN—but also corpus striatum, hippocampus, amygdala, thalamus and DN—demyelination may have modulated QSM but again, this is only speculation at the present time. It is interesting, additionally, that most of these structures (except STN, GP and amygdala) also returned significantly smaller age-related differences for signed—relative to absolute—QSM values, which also suggests

that the diamagnetic component in age-related magnetic susceptibility effects might not be negligible.

In contrast, both absolute and signed QSM, revealed superior sensitivity in detecting age-related differences in the thalamus: increased susceptibility in posterior, medial and anterior sub-nuclei; decreased, in the lateral group (Figs. 6 and 7). With the exception of the pulvinar, however, no such differences (increase or decrease) were observed with R_2*. These findings are in keeping with a previous study that showed QSM to be superior to R_2* in delineating thalamic sub-nuclei (Deistung et al., 2013). Moreover, recent findings have shown an age-related decrease in MT in the thalamus (Callaghan et al., 2014), thought to reflect concomitant demyelination, which may also be an indication that QSM is a superior contrast to capture such phenomenon.

The impact of age on myelination status is complex to interpret since whilst myelin sheaths are seen to degenerate with age, the process of myelin production continues throughout life (Peters, 2002). Furthermore, oligodendrocytes are essential for the production and maintenance of myelin and require iron to sustain their metabolic rate and facilitate synthesis of lipids and cholesterol (Bartzokis, 2011; Todorich et al., 2009). Under normal conditions, oligodendrocytes strongly stain for iron in the human brain (Connor et al., 1990; Gerber and Connor, 1989; LeVine, 1997; Morris et al., 1992). However, conditions that lead to iron elevation i.e. aging, are also associated with demyelination, since iron is released by damaged oligodendrocytes (Zecca et al., 2004). Therefore, some of the age-related differences detected with QSM may reflect oligodendrocytic alterations, but also the degree of myelination due to the determinative role of oligodendrocytes on myelin status. Future studies combining whole brain QSM with MT, or techniques to model the contributions of myelin and iron in MRI tissue contrasts (Stüber et al., 2014) would be highly desirable to clarify whether the present QSM/R_2* differential behaviors are driven by demyelination, calcification or some other process.

The strength of the whole-brain approach presented here is that it identified age-related phenomena beyond those in pre-determined ROIs. The most striking QSM behaviour was an extensive effect in the dorsal frontal lobe, particular in the motor cortices but also bilateral insula and cerebellar cortex. Additionally, QSM effects in superior frontal regions were not restricted to GM, revealing extensive age-related differences in WM. In stark contrast, the R_2* whole-brain analysis revealed no such effects in cerebral WM except for very focal effects in the fornix, which could be artefactual due to its small size and proximity to CSF, and cerebral/cerebellar peduncles. This would suggest the extensive age-related differences in WM with QSM could be due to its superior sensitivity to combined myelin/iron alterations but it could also be artefactual as previously discussed. However, one should note that a recent aging study reporting an age-related decrease in frontal WM using MT supports the validity of the former hypothesis (Callaghan et al., 2014).

Turning to GM, an interesting finding was that the human cortex in older adults appeared to mineralise unevenly. This is an important result because seminal

work from Hallgren and Sourander (1958) but also *in vivo* evidence using T_2* (Hasan et al., 2012), has suggested that there might be a graded behaviour across cerebral lobes, i.e. greatest iron deposition as a function of age in motor cortex, followed by occipital, parietal, temporal and finally, prefrontal regions. While this might hold true globally, the present whole-brain data also revealed that iron accumulation in older adults might be more focally specific than anticipated. Evidence supporting this observation was that cortical structures across all lobes were between those that returned the strongest age-related differences both using absolute QSM and R_2*. An exception – analogous to that observed in the GP but opposite to that in the thalamus – is that QSM, but not R2*, remained relatively unchanged across the occipital cortex. We have no explanation for this behaviour at present time, though it might be that studying the differential aging effects returned by these three structures (i.e. seemingly different biological scenarios) might offer some clues to deepen knowledge on the interplay between fundamental magnetic properties in biological tissue.

It is important to note several limitations on interpretation of these findings. First, we can only infer age-related differences from a cross-sectional study and cannot comment on lifespan trajectories of brain mineralisation – an interesting area for future research. Second, we must also acknowledge that our sample size (N=40) may have limited our ability to detect age-related QSM/R_2* sensitivity differences; however, it is reassuring the QSM effects reported here are highly concordant with those from a recent 3T QSM study in a much larger cohort (Acosta-Cabronero et al., 2016). Third, the reliability analysis revealed ICCs in the DN, SN and STN were below the typical guideline of reliability - ICC > 0.85, thus age-related differences reported in these regions should be interpreted with caution at present. As such, the relative attenuation of STN values with QSM compared to R_2* for example, may be due to the differential unreliability of these two measures in this region. Equally, differential effects between QSM and R_2* observed in the cortex may also be driven by low measurement reliability and whilst unlikely, it could also have contributed to the lack of pallidal effects with QSM. Generally differential unreliability must also be considered in accounting for contrasting QSM and R2* effects. Fourth, ROI extractions taken from small regions of the cortex may be more prone to systematic error as the accuracy of quantified susceptibility decreases when the size of the structure of interest is small (Hsieh et al., 2015), which may be exacerbated in older subjects with age-related atrophy. However it is highly unlikely atrophy alone is driving effects observed in cortical regions since taken as a whole, group differences cannot be explained in terms of global atrophy. Fifth, the markedly reduced age-related QSM/R_2* effects in the ventral PFC compared to dorsal regions may reflect relative sparing, however this may be a technical constraint due to signal loss in areas close to air/bone interfaces such as the ventral PFC which lies directly above the nasal cavity. Finally, it must be noted that QSM may also be implemented using single-echo susceptibility weighted scans (Acosta-Cabronero et al., 2013; Deistung et al., 2013). Single-echo QSM is an attractive method – the inherently improved signal-to-noise ratio at ultra-high field allows for higher spatial resolution, shorter echo times (since phase scales linearly with B_0×TE), reducing repetition time and ultimately, scan time, which can be reduced further with parallel imaging techniques. It is currently unclear, however, how the

present whole-brain findings may compare to higher resolution QSM maps derived from such acquisitions, particularly in regions where R_2* demonstrated superior sensitivity with the present multi-GRE acquisition.

5. CONCLUSIONS

In vivo high-resolution QSM using ultra-high field MRI and a relatively unbiased whole-brain analysis approach is a useful tool for assessing subtle variations in tissue composition and microstructure. The present study demonstrated QSM can potentially advance our current understanding of iron dysregulation in aging and related disorders; but also showed that combining QSM and R_2* using multi-GRE imaging can provide a more complete picture of mineralisation and demyelination in the aging human brain. To take this forward, it will be critical to understand what drives certain brain regions, most notably the GP, thalamus and occipital cortex, to exhibit different behaviour with the two techniques.

6. ACKWNOWLDEGMENTS

We thank Iris Mann and Anne Hochkeppler for their help with subject recruitment and local radiographers Denise Scheermann and Renate Blobel for their dedicated efforts in scanning standardisation and quality assurance. We would also like to thank Dr Shan Yang, Prof Oliver Speck and Dr Claus Tempelmann for their helpful input in the optimisation of shimming and parallel reconstruction for 7T MRI. We gratefully acknowledge the Leibniz Institute of Neurobiology for providing access to their 7T MR scanner. This work was supported by the SFB 779-TP A07.

7. REFERENCES

Acosta-Cabronero, J., Betts, M.J., Cardenas-Blanco, A., Yang, S., Nestor, P.J., 2016. In Vivo MRI Mapping of Brain Iron Deposition across the Adult Lifespan. J. Neurosci. 36, 364–374. doi:10.1523/JNEUROSCI.1907-15.2016

Acosta-Cabronero, J., Hall, L.D., 2009. Measurements by MRI of the settling and packing of solid particles from aqueous suspensions. AIChE J. 55, 1426–1433. doi:10.1002/aic.11754

Acosta-Cabronero, J., Williams, G.B., Cardenas-Blanco, A., Arnold, R.J., Lupson, V., Nestor, P.J., 2013. In Vivo Quantitative Susceptibility Mapping (QSM) in Alzheimer's Disease. PLoS ONE 8, e81093. doi:10.1371/journal.pone.0081093

Anik, Y., Iseri, P., Demirci, A., Komsuoglu, S., Inan, N., 2007. Magnetization transfer ratio in early period of Parkinson disease. Acad. Radiol. 14 (2), 189–192.

Avants, B., Epstein, C., Grossman, M., Gee, J., 2008. Symmetric diffeomorphic image registration with cross-correlation: Evaluating automated labeling of elderly and neurodegenerative brain. Med. Image Anal. 12, 26–41. doi:10.1016/j.media.2007.06.004

Barbosa, J.H.O., Santos, A.C., Tumas, V., Liu, M., Zheng, W., Haacke, E.M., Garrido Salmon, C.E., 2015. Quantifying Brain Iron Deposition in Patients with

Parkinson's Disease Using Quantitative Susceptibility Mapping, R2 and R2*. Magn. Reson. Imaging. doi:10.1016/j.mri.2015.02.021
Bartzokis, G., Cummings, J.L., Markham, C.H., Marmarelis, P.Z., Treciokas, L.J., Tishler, T.A., Marder, S.R., Mintz, J., 1999. MRI evaluation of brain iron in earlier- and later-onset Parkinson's disease and normal subjects. Magn Reson Imaging 17:213-222.
Bartzokis, G., Sultzer, D., Cummings, J., Holt, L.E., Hance, D.B., Henderson, V.W., Mintz, J., 2000. In vivo evaluation of brain iron in Alzheimer disease using magnetic resonance imaging. Arch Gen Psychiatry 57:47-53.
Bartzokis, G., 2011. Alzheimer's disease as homeostatic responses to age-related myelin breakdown. Neurobiol. Aging 32, 1341–1371. doi:10.1016/j.neurobiolaging.2009.08.007
Bartzokis, G., Tishler, T.A., Lu, P.H., Villablanca, P., Altshuler, L.L., Carter, M., Huang, D., Edwards, N., Mintz, J., 2007. Brain ferritin iron may influence age- and gender-related risks of neurodegeneration. Neurobiol. Aging 28, 414–423. doi:10.1016/j.neurobiolaging.2006.02.005
Bilgic, B., Pfefferbaum, A., Rohlfing, T., Sullivan, E.V., Adalsteinsson, E., 2012. MRI estimates of brain iron concentration in normal aging using quantitative susceptibility mapping. NeuroImage 59, 2625–2635. doi:10.1016/j.neuroimage.2011.08.077
Bunzeck, N., Singh-Curry, V., Eckart, C., Weiskopf, N., Perry, R.J., Bain, P.G., Düzel, E., Husain, M., 2013. Motor phenotype and magnetic resonance measures of basal ganglia iron levels in Parkinson's disease. Parkinsonism Relat. Disord. doi:10.1016/j.parkreldis.2013.08.011
Callaghan, M.F., Freund, P., Draganski, B., Anderson, E., Cappelletti, M., Chowdhury, R., Diedrichsen, J., FitzGerald, T.H.B., Smittenaar, P., Helms, G., Lutti, A., Weiskopf, N., 2014. Widespread age-related differences in the human brain microstructure revealed by quantitative magnetic resonance imaging. Neurobiol. Aging. doi:10.1016/j.neurobiolaging.2014.02.008
Cardenas-Blanco, A., Tejos, C., Irarrazaval, P., Cameron, I., 2008. Noise in Magnitude Magentic Resonance Images. Concepts in MR 32: 409-416
Cass, W.A., Grondin, R., Andersen, A.H., Zhang, Z., Hardy, P.A., Hussey-Andersen, L.K., Rayens, W.S., Gerhardt, G.A., Gash, D.M., 2007. Iron accumulation in the striatum predicts aging-related decline in motor function in rhesus monkeys. Neurobiol. Aging 28, 258–271. doi:10.1016/j.neurobiolaging.2005.12.010
Chen, W., Zhu, W., Kovanlikaya, Ii., Kovanlikaya, A., Liu, T., Wang, S., Salustri, C., Wang, Y., 2014. Intracranial calcifications and hemorrhages: characterization with quantitative susceptibility mapping. Radiology 270, 496–505.
Connor, J.R., Menzies, S.L., St Martin, S.M., Mufson, E.J., 1990. Cellular distribution of transferrin, ferritin, and iron in normal and aged human brains. J. Neurosci. Res. 27, 595–611.
Cornett, C.R., Markesbery, W.R., Ehmann, W.D., 1998. Imbalances of trace elements related to oxidative damage in Alzheimer's disease brain. Neurotoxicology 19:339-345.
Daugherty, A., Raz, N., 2013. Age-related differences in iron content of subcortical nuclei observed in vivo: A meta-analysis. NeuroImage 70, 113–121. doi:10.1016/j.neuroimage.2012.12.040

Daugherty, A.M., Haacke, E.M., Raz, N., 2015. Striatal Iron Content Predicts Its Shrinkage and Changes in Verbal Working Memory after Two Years in Healthy Adults. J. Neurosci. 35, 6731–6743. doi:10.1523/JNEUROSCI.4717-14.2015

de Rochefort, L., Brown, R., Prince, M.R., Wang, Y., 2008. Quantitative MR susceptibility mapping using piece-wise constant regularized inversion of the magnetic field. Magn. Reson. Med. 60, 1003–1009. doi:10.1002/mrm.21710

Deistung, A., Schäfer, A., Schweser, F., Biedermann, U., Turner, R., Reichenbach, J.R., 2013. Toward in vivo histology: A comparison of quantitative susceptibility mapping (QSM) with magnitude-, phase-, and $R2_*$-imaging at ultra-high magnetic field strength. NeuroImage 65, 299–314. doi:10.1016/j.neuroimage.2012.09.055

Draganski, B., Ashburner, J., Hutton, C., Kherif, F., Frackowiak, R.S.J., Helms, G., Weiskopf, N., 2011. Regional specificity of MRI contrast parameter changes in normal ageing revealed by voxel-based quantification (VBQ). NeuroImage 55, 1423–1434. doi:10.1016/j.neuroimage.2011.01.052

Fazekas, F., Chawluk, J.B., Alavi, A., Hurtig, H.I., Zimmerman ,R.A., 1987. MR signal abnormalities at 1.5 T in Alzheimer's dementia and normal aging. AJR Am J Roentgenol 149:351–356.

Fernández-Seara, M.A., Wehrli, F.W., 2000. Postprocessing technique to correct for background gradients in image-based R*(2) measurements. Magn. Reson. Med. 44 (3), 358–366

Fukunaga, M., Li, T.-Q., van Gelderen, P., de Zwart, J.A., Shmueli, K., Yao, B., Lee, J., Maric, D., Aronova, M.A., Zhang, G., Leapman, R.D., Schenck, J.F., Merkle, H., Duyn, J.H., 2010. Layer-specific variation of iron content in cerebral cortex as a source of MRI contrast. Proc. Natl. Acad. Sci. 107, 3834–3839. doi:10.1073/pnas.0911177107

Gelman, N., Gorell, J.M., Barker, P.B., Savage, R.M., Spickler, E.M., Windham, J.P., Knight, R.A., 1999. MR imaging of human brain at 3.0 T: preliminary report on transverse relaxation rates and relation to estimated iron content. Radiology 210, 759–767.

Gerber, M.R., Connor, J.R., 1989. Do oligodendrocytes mediate iron regulation in the human brain? Ann. Neurol. 26, 95–98. doi:10.1002/ana.410260115

Ghadery, C., Pirpamer, L., Hofer, E., Langkammer, C., Petrovic, K., Loitfelder, M., Schwingenschuh, P., Seiler, S., Duering, M., Jouvent, E., Schmidt, H., Fazekas, F., Mangin, J.-F., Chabriat, H., Dichgans, M., Ropele, S., Schmidt, R., 2015. R2* mapping for brain iron: associations with cognition in normal aging. Neurobiol. Aging 36, 925–932. doi:10.1016/j.neurobiolaging.2014.09.013

Gudbjartsson, H., Patz, S., 1995. The Rician distribution of noisy MRI data. Magn. Reson. Med. 34, 910–914.

Haacke, E.M., Ayaz, M., Khan, A., Manova, E.S., Krishnamurthy, B., Gollapalli, L., Ciulla, C., Kim, I., Petersen, F., Kirsch, W., 2007. Establishing a baseline phase behavior in magnetic resonance imaging to determine normal vs. abnormal iron content in the brain. J. Magn. Reson. Imaging 26, 256–264.

Haacke, E.M., Liu, S., Buch, S., Zheng, W., Wu, D., Ye, Y., 2015. Quantitative susceptibility mapping: current status and future directions. Magn. Reson. Imaging 33, 1–25. doi:10.1016/j.mri.2014.09.004

Hallgren, B., Sourander, P., 1958. The effect of age on the non-haemin iron in the human brain. J. Neurochem. 3, 41–51.
Hasan, K.M., Walimuni, I.S., Kramer, L.A., Narayana, P.A., 2012. Human brain iron mapping using atlas-based T2 relaxometry. Magn. Reson. Med. 67, 731–739. doi:10.1002/mrm.23054
Hsieh, C.-Y., Cheng, Y.-C.N., Xie, H., Haacke, E.M., Neelavalli, J., 2015. Susceptibility and size quantification of small human veins from an MRI method. Magn. Reson. Imaging 33, 1191–1204. doi:10.1016/j.mri.2015.07.008
Ide, S., Kakeda, S., Ueda, I., Watanabe, K., Murakami, Y., Moriya, J., Ogasawara, A., Futatsuya, K., Sato, T., Ohnari, N., Okada, K., Matsuyama, A., Fujiwara, H., Hisaoka, M., Tsuji, S., Liu, T., Wang, Y., Korogi, Y., 2015. Internal structures of the globus pallidus in patients with Parkinson's disease: evaluation with quantitative susceptibility mapping (QSM). Eur. Radiol. 25, 710–718. doi:10.1007/s00330-014-3472-7
Jack, C.R., Twomey, C.K., Zinsmeister, A.R., Sharbrough, F.W., Petersen, R.C., Cascino, G.D., 1989. Anterior temporal lobes and hippocampal formations: normative volumetric measurements from MR images in young adults. Radiology. 1989 Aug;172(2):549-54.
Klein, A., Tourville, J., 2012. 101 Labeled Brain Images and a Consistent Human Cortical Labeling Protocol. Front. Neurosci. 6. doi:10.3389/fnins.2012.00171
Langkammer, C., Krebs, N., Goessler, W., Scheurer, E., Ebner, F., Yen, K., Fazekas, F., Ropele, S., 2010. Quantitative MR Imaging of Brain Iron: A Postmortem Validation Study 1. Radiology 257, 455–462.
Langkammer, C., Schweser, F., Krebs, N., Deistung, A., Goessler, W., Scheurer, E., Sommer, K., Reishofer, G., Yen, K., Fazekas, F., Ropele, S., Reichenbach, J.R., 2012. Quantitative susceptibility mapping (QSM) as a means to measure brain iron? A post mortem validation study. NeuroImage 62, 1593–1599. doi:10.1016/j.neuroimage.2012.05.049
Lee, J., Shmueli, K., Kang, B.-T., Yao, B., Fukunaga, M., van Gelderen, P., Palumbo, S., Bosetti, F., Silva, A.C., Duyn, J.H., 2012. The contribution of myelin to magnetic susceptibility-weighted contrasts in high-field MRI of the brain. NeuroImage 59, 3967–3975. doi:10.1016/j.neuroimage.2011.10.076
Lee, J.E., Chung, M.K., Lazar, M., DuBray, M.B., Kim, J., Bigler, E.D., Lainhart, J.E., Alexander, A.L., 2009. A study of diffusion tensor imaging by tissue-specific, smoothing-compensated voxel-based analysis. NeuroImage 44, 870–883. doi:10.1016/j.neuroimage.2008.09.041
LeVine, S.M., 1997. Iron deposits in multiple sclerosis and Alzheimer's disease brains. Brain Res. 760, 298–303.
Li, W., Langkammer, C., Chou, Y.-H., Petrovic, K., Schmidt, R., Song, A.W., Madden, D.J., Ropele, S., Liu, C., 2015. Association between increased magnetic susceptibility of deep gray matter nuclei and decreased motor function in healthy adults. NeuroImage 105, 45–52. doi:10.1016/j.neuroimage.2014.10.009
Li, W., Wu, B., Avram, A.V., Liu, C., 2012. Magnetic susceptibility anisotropy of human brain in vivo and its molecular underpinnings. NeuroImage 59, 2088–2097. doi:10.1016/j.neuroimage.2011.10.038
Li, W., Wu, B., Batrachenko, A., Bancroft-Wu, V., Morey, R.A., Shashi, V., Langkammer, C., De Bellis, M.D., Ropele, S., Song, A.W., Liu, C., 2014.

Differential developmental trajectories of magnetic susceptibility in human brain gray and white matter over the lifespan: Brain Magnetic Susceptibility Over Lifespan. Hum. Brain Mapp. 35, 2698–2713. doi:10.1002/hbm.22360
Liu, C., 2010. Susceptibility tensor imaging. Magn. Reson. Med. 63, 1471–1477. doi:10.1002/mrm.22482
Liu, C., Li, W., Johnson, G.A., Wu, B., 2011. High-field (9.4T) MRI of brain dysmyelination by quantitative mapping of magnetic susceptibility. NeuroImage 56, 930–938. doi:10.1016/j.neuroimage.2011.02.024
Liu, T., Wisnieff, C., Lou, M., Chen, W., Spincemaille, P., Wang, Y., 2013. Nonlinear formulation of the magnetic field to source relationship for robust quantitative susceptibility mapping. Magn. Reson. Med. 69, 467–476. doi:10.1002/mrm.24272
Lotfipour, A.K., Wharton, S., Schwarz, S.T., Gontu, V., Schäfer, A., Peters, A.M., Bowtell, R.W., Auer, D.P., Gowland, P.A., Bajaj, N.P.S., 2012. High resolution magnetic susceptibility mapping of the substantia nigra in Parkinson's disease. J. Magn. Reson. Imaging.
Mori, S., Oishi, K., Jiang, H., Jiang, L., Li, X., Akhter, K., Hua, K., Faria, A.V., Mahmood, A., Woods, R., Toga, A.W., Pike, G.B., Neto, P.R., Evans, A., Zhang, J., Huang, H., Miller, M.I., van Zijl, P., Mazziotta, J., 2008. Stereotaxic white matter atlas based on diffusion tensor imaging in an ICBM template. NeuroImage 40, 570–582. doi:10.1016/j.neuroimage.2007.12.035
Morozov, V.A., 1966. On the solution of functional equations by the method of regularization. Soviet Math Dokl 7:414-417.
Morris, C.M., Candy, J.M., Oakley, A.E., Bloxham, C.A., Edwardson, J.A., 1992. Histochemical Distribution of Non-Haem Iron in the Human Brain. Cells Tissues Organs 144, 235–257. doi:10.1159/000147312
Patenaude, B., Smith, S.M., Kennedy, D.N., Jenkinson, M., 2011. A Bayesian model of shape and appearance for subcortical brain segmentation. NeuroImage 56, 907–922. doi:10.1016/j.neuroimage.2011.02.046
Pengas, G., Pereira, J.M., Williams, G.B., Nestor, P.J., 2009. Comparative reliability of total intracranial volume estimation methods and the influence of atrophy in a longitudinal semantic dementia cohort. J Neuroimaging Jan;19(1):37-46
Penke, L., Valdés Hernandéz, M.C., Maniega, S.M., Gow, A.J., Murray, C., Starr, J.M., Bastin, M.E., Deary, I.J., Wardlaw, J.M., 2012. Brain iron deposits are associated with general cognitive ability and cognitive aging. Neurobiol. Aging 33, 510–517.e2. doi:10.1016/j.neurobiolaging.2010.04.032
Péran, P., Cherubini, A., Luccichenti, G., Hagberg, G., Démonet, J.-F., Rascol, O., Celsis, P., Caltagirone, C., Spalletta, G., Sabatini, U., 2009. Volume and iron content in basal ganglia and thalamus. Hum. Brain Mapp. 30, 2667–2675. doi:10.1002/hbm.20698
Pereira, J.M.S., Xiong, L., Acosta-Cabronero, J., Pengas, G., Williams, G.B., Nestor, P.J., 2010. Registration accuracy for VBM studies varies according to region and degenerative disease grouping. NeuroImage 49, 2205–2215. doi:10.1016/j.neuroimage.2009.10.068
Peters, A., 2002. The effects of normal aging on myelin and nerve fibers: a review. J. Neurocytol. 31, 581–593.

Pfefferbaum, A., Adalsteinsson, E., Rohlfing, T., Sullivan, E.V., 2009. MRI estimates of brain iron concentration in normal aging: Comparison of field-dependent (FDRI) and phase (SWI) methods. NeuroImage 47, 493–500. doi:10.1016/j.neuroimage.2009.05.006

Poynton, C.B., Jenkinson, M., Adalsteinsson, E., Sullivan, E.V., Pfefferbaum, A., Wells III, W., 2015. Quantitative Susceptibility Mapping by Inversion of a Perturbation Field Model: Correlation With Brain Iron in Normal Aging. IEEE Trans. Med. Imaging 34, 339–353. doi:10.1109/TMI.2014.2358552

Ramos, P., Santos, A., Pinto, N.R., Mendes, R., Magalhães, T., Almeida, A., 2014. Iron levels in the human brain: A post-mortem study of anatomical region differences and age-related changes. J. Trace Elem. Med. Biol. 28, 13–17. doi:10.1016/j.jtemb.2013.08.001

Raz, N., Rodrigue, K.M., Haacke, E.M., 2007. Brain Aging and Its Modifiers: Insights from in Vivo Neuromorphometry and Susceptibility Weighted Imaging. Ann. N. Y. Acad. Sci. 1097, 84–93. doi:10.1196/annals.1379.018

Reichenbach, J.R., Schweser, F., Serres, B., Deistung, A., 2015. Quantitative Susceptibility Mapping: Concepts and Applications. Clin. Neuroradiol. doi:10.1007/s00062-015-0432-9

Rodrigue, K.M., Daugherty, A.M., Haacke, E.M., Raz, N., 2013. The Role of Hippocampal Iron Concentration and Hippocampal Volume in Age-Related Differences in Memory. Cereb. Cortex 23, 1533–1541. doi:10.1093/cercor/bhs139

Rodrigue, K.M., Haacke, E.M., Raz, N., 2011. Differential effects of age and history of hypertension on regional brain volumes and iron. NeuroImage 54, 750–759. doi:10.1016/j.neuroimage.2010.09.068

Schaltenbrand, G., Wahren, W., Hassler, R., 1977. Atlas for Stereotaxy of the Human Brain. Georg Thieme Verlag

Schofield, M.A., Zhu, Y., 2003. Fast phase unwrapping algorithm for interferometric applications. Opt Lett 28:1194-1196.

Schweser, F., Deistung, A., Lehr, B.W., Reichenbach, J.R., 2011. Quantitative imaging of intrinsic magnetic tissue properties using MRI signal phase: An approach to in vivo brain iron metabolism? NeuroImage 54, 2789–2807. doi:10.1016/j.neuroimage.2010.10.070

Smith, S., Nichols, T., 2009. Threshold-free cluster enhancement: Addressing problems of smoothing, threshold dependence and localisation in cluster inference. NeuroImage 44, 83–98. doi:10.1016/j.neuroimage.2008.03.061

Smith, S.M., 2002. Fast robust automated brain extraction. Hum. Brain Mapp. 17, 143–155. doi:10.1002/hbm.10062

Sofic, E., Paulus, W., Jellinger, K., Riederer, P., Youdim, MB., 1991. Selective increase of iron in substantia nigra zona compacta of parkinsonian brains. J Neurochem 56:978-982.

Stüber, C., Morawski, M., Schäfer, A., Labadie, C., Wähnert, M., Leuze, C., Streicher, M., Barapatre, N., Reimann, K., Geyer, S., Spemann, D., Turner, R., 2014. Myelin and iron concentration in the human brain: A quantitative study of MRI contrast. NeuroImage 93, 95–106. doi:10.1016/j.neuroimage.2014.02.026

Sullivan, E.V., Adalsteinsson, E., Rohlfing, T., Pfefferbaum, A., 2009. Relevance of Iron Deposition in Deep Gray Matter Brain Structures to Cognitive and Motor Performance in Healthy Elderly Men and Women: Exploratory

Findings. Brain Imaging Behav. 3, 167–175. doi:10.1007/s11682-008-9059-7
Sun, H., Walsh, A.J., Lebel, R.M., Blevins, G., Catz, I., Lu, J.-Q., Johnson, E.S., Emery, D.J., Warren, K.G., Wilman, A.H., 2015. Validation of quantitative susceptibility mapping with Perls' iron staining for subcortical gray matter. NeuroImage 105, 486–492. doi:10.1016/j.neuroimage.2014.11.010
Todorich, B., Pasquini, J.M., Garcia, C.I., Paez, P.M., Connor, J.R., 2009. Oligodendrocytes and myelination: The role of iron. Glia 57, 467–478. doi:10.1002/glia.20784
Tustison, N.J., Avants, B.B., Cook, P.A., Yuanjie Zheng, Egan, A., Yushkevich, P.A., Gee, J.C., 2010. N4ITK: Improved N3 Bias Correction. IEEE Trans. Med. Imaging 29, 1310–1320. doi:10.1109/TMI.2010.2046908
Ward, R.J., Zucca, F.A., Duyn, J.H., Crichton, R.R., Zecca, L., 2014. The role of iron in brain ageing and neurodegenerative disorders. Lancet Neurol. 13, 1045–1060.
Winkler, A.M., Ridgway, G.R., Webster, M.A., Smith, S.M., Nichols, T.E., 2014. Permutation inference for the general linear model. NeuroImage 92, 381–397. doi:10.1016/j.neuroimage.2014.01.060
Yao, B., Li, T., Gelderen, P., Shmueli, K., Dezwart, J., Duyn, J., 2009. Susceptibility contrast in high field MRI of human brain as a function of tissue iron content. NeuroImage 44, 1259–1266. doi:10.1016/j.neuroimage.2008.10.029
Zecca, L., Youdim, M.B.H., Riederer, P., Connor, J.R., Crichton, R.R., 2004. Iron, brain ageing and neurodegenerative disorders. Nat. Rev. Neurosci. 5, 863–873. doi:10.1038/nrn1537
Zheng, W., Nichol, H., Liu, S., Cheng, Y.-C.N., Haacke, E.M., 2013. Measuring iron in the brain using quantitative susceptibility mapping and X-ray fluorescence imaging. NeuroImage 78, 68–74. doi:10.1016/j.neuroimage.2013.04.022